

Experimental characterization of GNSS carrier phase diffraction errors in a controlled environment

Downloaded from: https://research.chalmers.se, 2026-10-18 09:34 UTC

Citation for the original published paper (version of record):
Dutta, U., Johansson, J., Haas, R. et al (2026). Experimental characterization of GNSS carrier phase diffraction errors in a controlled
environment. GPS Solutions, 30(4). http://dx.doi.org/10.1007/s10291-026-02138-1

N.B. When citing this work, cite the original published paper.

research.chalmers.se offers the possibility of retrieving research publications produced at Chalmers University of Technology. It covers all kind of research output: articles, dissertations, conference papers, reports etc. since 2004. research.chalmers.se is administrated and maintained by Chalmers Library

(article starts on next page)

GPS Solutions (2026) 30:195
https://doi.org/10.1007/s10291-026-02138-1

RESEARCH

Experimental characterization of GNSS carrier phase diffraction errors in a controlled environment

Uttama Dutta[1,2] · Jan M. Johansson[1,2] · Rüdiger Haas[1] · Sten E. G. Bergstrand[2] · Carsten Rieck[2]

Received: 18 December 2025 / Accepted: 19 August 2026
© The Author(s) 2026

Abstract

This study presents a rigorous analysis of signal diffraction, a pervasive yet often overlooked error source in high-precision GNSS positioning. The research uses a controlled environment and an extensive data set. Using a movable wall of constant height, we demonstrate that diffraction impact is inversely proportional to the obstacle distance, with errors at 1 m distance far exceeding those at 3 m. Position estimates from Precise Point Positioning (PPP) analysis and residuals from double difference analysis were used to show the effect on geodetic results. The study further validates the physical diffraction mechanism through signal-to-noise ratio (SNR) data using a Knife-edge diffraction (KED) model. It is seen that, while the KED model works well for horizontal distances of 2 m, in the near field of the antenna, the model requires improvement to explain observed SNR anomalies. Further, we show that signal disturbance commences when an obstacle intrudes upon the first Fresnel zone, even while it remains below the direct line-of-sight. The results conclusively demonstrate that low-elevation satellites suffer the most severe diffraction effects due to their longer propagation paths through the diffracted field. Consequently, based on our extensive data processing and analysis, we propose practical guidelines for field operations. It is recommended (subject to constraints) to ensure that the obstructive environment does not subtend an angle greater than 11° on the antenna. This would help preserve data quality in demanding applications like PPP and Real Time Kinematic (RTK).

Keywords GNSS · Diffraction · Fresnel zones · PPP · RTK · SNR

Introduction

GNSS is a cornerstone for modern geodesy and precise positioning. However, the performance of GNSS, like any other technique, is prone to various error sources. Atmospheric errors may arise from the troposphere or ionosphere. Space segment errors include issues related to satellite orbits, clock inaccuracies, antenna center variations, relativistic effects, and phase windup. User segment errors can stem from diffraction, multipath effects, antenna phase center variations, receiver clock errors, and noise. Techniques such as post-processed Precise Point Positioning (PPP) and Real Time Kinematic (RTK) enable centimeter-level accuracy by leveraging sophisticated models to correct for well-understood error sources. Scientific software packages like the Bernese GNSS Software (BSW) (Dach et al. 2015) and GipsyX (Bertiger et al. 2020) implement these models to mitigate the majority of these systematic errors in post-processing.

✉ Uttama Dutta
uttama@chalmers.se; uttama.dutta@ri.se

Jan M. Johansson
jan.johansson@chalmers.se

Rüdiger Haas
rudiger.haas@chalmers.se

Sten E. G. Bergstrand
sten.bergstrand@ri.se

Carsten Rieck
carsten.rieck@ri.se

[1] Department of Physics and Astronomy, Chalmers University of Technology, Onsala Space Observatory, SE-439 92 Onsala, Sweden

[2] Department of Measurement Science and Technology, RISE Research Institutes of Sweden, Brinellgatan 4, SE-504 62 Borås, Sweden

However, local environmental effects at the receiver antenna remain a significant challenge. In obstructed environments like urban canyons or near large machinery (such as excavators and other construction equipment), the direct line-of-sight (LOS) signal is often lost. The antenna instead receives a combination of reflected (multipath) and diffracted signals, which are not modeled by standard software and can degrade positioning accuracy substantially. While multipath is a widely recognized issue, diffraction—the bending of signals around obstacles—is a critical but less studied phenomenon.

Diffraction occurs when waves encounter edges, apertures and screens and introduce additional path delay (Dutta et al. 2026; Dutta and Johansson 2023; Bradbury 2007). This delay, typically at the centimeter to decimeter level (Mcgraw et al. 2020), can cause significant phase fluctuations, amplitude attenuation, and even cycle slips (Breitsch et al. 2020). This can significantly degrade the GNSS signal resulting in poor positioning performance, especially in dense urban areas (Zhang and Hsu 2021). Recent studies have quantified its impact, showing signal strength losses up to 17 dB-Hz (Schaper et al. 2022). Various modeling approaches have been explored, including the Knife-edge diffraction (KED) model, the Uniform Geometrical Theory of Diffraction (UTD) and the 3D building models (Zhang and Hsu 2021; Fan and Ding 2006; Nicolás et al. 2012; Panicciari et al. 2017; Suzuki and Kubo 2012). Brunner et al. (1999) developed a stochastic SIGMA-Δ model for GPS signal diffraction using signal-to-noise ratio (SNR) as their primary parameter for the demonstration of diffraction.

A common strategy for mitigating these local effects is to identify and exclude non-line-of-sight (NLOS) signals. Methods include using obstruction-adaptive elevation masks (OAEMs) (Xi et al. 2023; Zimmermann et al. 2017), multipoint hemispherical grids (Zou et al. 2023), geographic cut-off elevations (Zhang et al. 2022; Ren et al. 2023), and 3D-mapping-aided algorithms. However, simply excluding NLOS signals can weaken the satellite geometry and degrade positioning (Xi et al. 2023; Zou et al. 2023; Groves and Jiang 2013). While these approaches address general signal degradation, they often treat multipath and diffraction as a combined problem. Xi et al. (2025) introduced a method to extract and model diffraction error, offering important empirical evidence that this error can exhibit monotonic trends and considerable magnitudes (50–200 mm). While their approach is geometrically based, incorporating the physics of wave diffraction and signal-quality metrics like SNR could enhance future models. Some elements of their proposed 'vertical diffraction' model may warrant further investigation. For example, the model indicates that error grows with the horizontal obstruction distance S, a relationship that may benefit from additional geometric context. The reported tendency for vertical error to be larger at high elevations than at low elevations–given the same S and diffraction angle–is also noteworthy and could be explored further in relation to established diffraction theory. Together, these observations suggest that continued work integrating physical propagation models may lead to a more comprehensive understanding of diffraction effects.

While recent studies have advanced our understanding of signal obstruction, the specific contribution of diffraction is often still treated alongside multipath. Clearly differentiating and quantifying the distinct signature of diffraction presents an important research opportunity. Such work is key to developing precise mitigation techniques especially for high-precision applications where even transient errors are critical. This research advances the investigation of GNSS signal diffraction by building upon the ideas introduced by Dutta et al. (2026), who demonstrated the use of post-fit carrier-phase residuals, position estimates, and SNR data to identify diffraction in real-world urban scenarios. However, their analysis relied on existing infrastructure where obstruction geometry could not be systematically varied or compared to a true unobstructed baseline. Their work provided important insights in a complex static environment. In contrast, this study expands the scope through a controlled experimental approach which isolates diffraction effects with greater precision and under quantifiable geometric conditions. We introduce a novel experimental setup involving a movable metallic wall, which enables the creation of five distinct diffraction scenarios with known ground truth. Each scenario is directly compared to an unobstructed reference case. Using dual-frequency PPP and single-frequency double-difference analysis, we systematically extract and evaluate diffraction-induced errors. The paper comprehensively documents the experimental environment, data acquisition, and processing methodology to support reproducibility. Among the key findings, we empirically confirm that PPP position errors can double when a diffracting wall is positioned at 1 m–a prediction originally made by Dutta et al. (2026) using simulated data–a prediction that lacked experimental verification until now. Further, we validate the earlier proposition that Dilution of Precision (DOP) alone is an insufficient metric for assessing positioning reliability in obstructed environments for all the five distinct cases. An important contribution of this work is the analysis of double-difference residuals, which exhibit a well-defined and geometrically consistent diffraction signature. This analysis provides a clearer interpretation of the residuals within the two-receiver, two-satellite puzzle than previously available, and offers a comparative assessment against theoretical diffraction computation. We show that diffraction causes systematic biases that impair ambiguity resolution in the post-processed solution. Additionally, we apply the KED

model to SNR observations, confirming its applicability at far-field distances while revealing its inadequacy for near-field obstructions at 1 m. Collectively, these results offer a rigorous, experiment-based confirmation and extension of earlier simulation-based claims, while introducing new methodologies and comparative analyses that deepen the understanding of the impact of diffraction to high-precision GNSS.

The paper begins with the theoretical background, covering diffraction physics, its impact on PPP processing, and the isolation of diffraction effects in carrier-phase residuals. The experimental setup and methodology then details the controlled environment, data collection, and processing techniques. The results section examines PPP position degradation, DOP metrics, double-difference network residuals, comparisons with theoretical values, SNR modeling via the KED loss model, and modifications to the knife-edge model. This is followed by the discussion, and the paper ends with the conclusions, which summarize findings and suggest future research directions.

Theoretical background

Physics of diffraction

Diffraction is the physical phenomenon that occurs when a radio wave encounters an obstacle or a sharp edge, causing the electromagnetic wave to bend around it and propagate into the shadow region. The attenuation in the signal strength obtained from satellites are a direct indicator of the diffractive fading. KED model is used to model this attenuation. Diffraction can also be studied using the difference in path length / range measurements between the Shortest Geometric Path (SGP) to the satellite and the bent NLOS path. The results obtained in this paper use signal strength measurements, range residuals and position estimates from experimental data to demonstrate the effect produced by a moving metallic wall.

The diffraction effects in this study are modeled using the classical KED framework (Orfanidis 2002). The accurate diffraction loss as a function of the Fresnel-Kirchhoff diffraction parameter ν is given in Dutta et al. (2026). An approximation to model the loss (L) in signal strength is provided by the Lee piece-wise model (Rappaport 1996). This approximate model is given by:

$$L = \begin{cases} 0 & \text{for all } \nu \le -1 \\ 20\log_{10}(0.5 - 0.62\nu) & \text{for all } -1 \le \nu \le 0 \\ 20\log_{10}(0.5e^{-0.95\nu}) & \text{for all } 0 \le \nu \le 1 \\ 20\log_{10}\left(0.4 - \sqrt{0.1184 - (0.38 - 0.1\nu)^2}\right) & \text{for all } 1 \le \nu \le 2.4 \\ 20\log_{10}\left(\frac{0.225}{\nu}\right) & \text{for all } \nu \ge 2.4 \end{cases} \quad (1)$$

The analysis using the KED model is similar to Dutta et al. (2026) and is used to understand the signal degradation in the vicinity of a GNSS antenna with SNR measurements.

Figure 1 shows the 3D view and the side view of a typical KED environment due to an obstructing wall near a GNSS antenna. The geometry in the vicinity of the GNSS antenna together with the NLOS and SGP path from a satellite at a specific azimuth are shown. In the case of GNSS, ν can be written as follows, as shown in Dutta et al. (2026):

$$\nu = h\sqrt{\frac{2}{\lambda R_0}} \quad (2)$$

where λ is the wavelength and R_0 is the distance of the knife edge obstruction from the receiver antenna, projected on the SGP to the satellite. Thus, one can compute the signal loss due to diffraction caused by the obstruction if the geometrical measurements R_0 (or d) and h are known for a specific receiver environment. From the side view of Fig. 1,

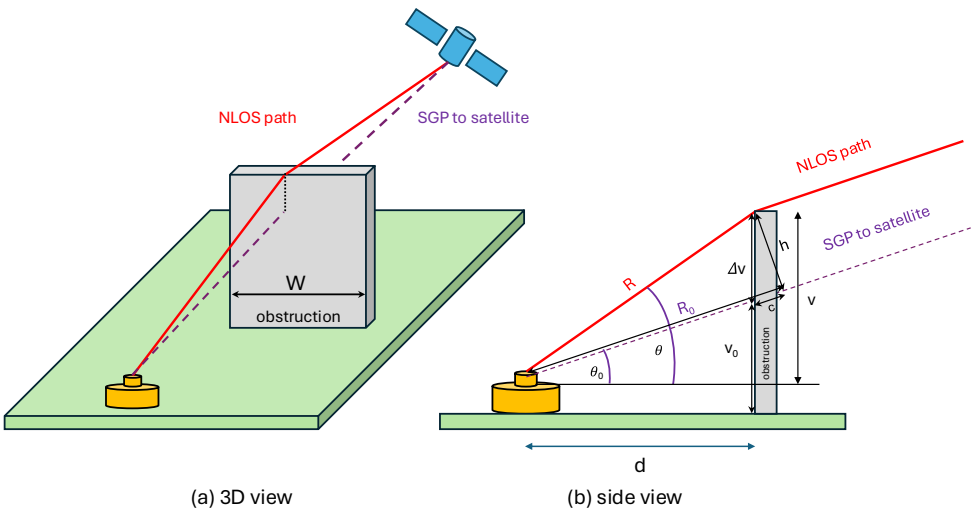


Fig. 1 Example geometry of a diffraction environment around a GNSS antenna. (**a**) 3D view (**b**) side view

the perpendicular distance between the SGP and the NLOS path, h, can be computed as

$$h = \Delta V \cos\theta_o = (V - d\ \tan\theta_o)\cos\theta_o, \tag{3}$$

where θ_o is the elevation angle to the satellite from the receiver. For the geometry of Fig. 1, the difference in path length can be computed as shown in Dutta and Johansson (2023) by using the following equations:

$$\Delta V = V - d \cdot \tan\theta_o \quad \text{and} \quad c = \Delta V \cdot \sin\theta_o \tag{4}$$

$$R = \sqrt{V^2 + d^2} \quad \text{and} \quad R_0 = \sqrt{(d \cdot \tan\theta_o)^2 + d^2} + c \tag{5}$$

The difference between R and R_0 is then the path length difference. The horizontal distance d to the wall is a function of the signal's azimuth ϕ. Given a shortest distance $d(\phi_0)$ at a reference azimuth ϕ_0, the distance at a different azimuth ϕ_1, $d(\phi_1)$, can be computed as shown by Dutta et al. (2026),

$$d(\phi_1) = \frac{d(\phi_0)}{\cos(\phi_1 - \phi_0)}. \tag{6}$$

For the geometrical relations shown in Fig. 1, the expected extra path delay for varying elevations θ_0, horizontal distances to the wall d and for a constant wall height V of 0.8 m are shown in Table 1. The wall has a constant width W of 1 m.

Different cases were considered, where the shortest distances to the wall are assumed to vary from 1 to 3 m in steps of 0.5 m at a reference azimuth, $\phi_0 = 199^o$. When the wall is close at 1 m, it casts a bigger shadow and extends from azimuth 171° to 225°. However at 1.5, 2, 2.5 and 3 m distance the shadow becomes smaller and therefore at 3 m the wall extends from 189° to 207°.

For a constant obstruction height $V = 0.8$ m, the elevation angle for grazing incidence, θ, was computed for each distance d. The elevation angle θ_0 was then varied from 0° to θ in 4° increments, and the azimuth was varied in 10°

Table 1 Computations of additional path delay due to diffraction for different geometries around a GNSS antenna are shown. For a constant obstruction height $V = 0.8$ m, the elevation angle for grazing incidence, θ was computed for each distance d. The elevation angle θ_0 was then varied from 0° to θ in 4° increments, and the azimuth was varied in 10° increments for each geometry

Path delay (m) when shortest distance to wall is 1 *m*										
Az/El ( )	0	4	8	12	16	20	24	28	32	36
171	0.254	0.201	0.154	0.112	0.077	0.049	0.027	0.011	0.002	
181	0.270	0.216	0.169	0.126	0.090	0.060	0.035	0.017	0.006	
191	0.278	0.225	0.177	0.134	0.097	0.066	0.040	0.021	0.008	0.001
201	0.280	0.227	0.179	0.136	0.099	0.067	0.042	0.022	0.009	0.001
211	0.276	0.222	0.174	0.132	0.095	0.064	0.039	0.020	0.007	0.001
221	0.264	0.211	0.163	0.122	0.086	0.056	0.032	0.015	0.004	
Path delay (m) when shortest distance to wall is 1.5 *m*										
Az/El ( )	0	4	8	12	16	20	24			
180	0.190	0.138	0.094	0.059	0.031	0.012	0.002			
190	0.198	0.146	0.101	0.065	0.036	0.016	0.004			
200	0.200	0.148	0.103	0.066	0.038	0.017	0.004			
210	0.197	0.145	0.100	0.064	0.035	0.015	0.003			
Path delay (m) when shortest distance to wall is 2 *m*										
Az/El ( )	0	4	8	12	16	20				
184	0.149	0.098	0.058	0.028	0.009					
194	0.154	0.103	0.062	0.031	0.011	0.001				
204	0.154	0.103	0.062	0.031	0.011	0.001				
212	0.150	0.100	0.059	0.029	0.009	0.001				
Path delay (m) when shortest distance to wall is 2.5 *m*										
Az/El ( )	0	4	8	12	16					
187	0.122	0.073	0.036	0.012	0.001					
197	0.125	0.075	0.038	0.013	0.001					
207	0.124	0.074	0.037	0.013	0.001					
209	0.123	0.073	0.036	0.012	0.001					
Path delay (m) when shortest distance to wall is 3 *m*										
Az/El ( )	0	4	8	12						
189	0.103	0.055	0.022	0.004						
199	0.105	0.056	0.023	0.004						
207	0.104	0.055	0.022	0.004						

increments for each configuration. The corresponding path delays were computed using equations 4 and 5.

As summarized in Table 1, the modeled path delay ranges from millimeter to decimeter. The results demonstrate that the delay increases as the elevation angle θ_0 decreases. Conversely, the delay decreases with a greater azimuth separation ($\phi_1 - \phi_0$) from the reference direction. This occurs because a larger azimuth separation effectively increases the distance d to the obstruction. For a constant V, this reduces the grazing angle θ, thereby reducing the obstruction's shadowing effect on the antenna.

The severity of the diffraction effect depends on the geometric configuration of the propagation path. Based on Eq. 1, no diffraction loss occurs when $\nu \leq -1$. This condition defines a critical obstacle height, h_c, below which diffraction has minimal impact. Solving for the height that satisfies $\nu = -1$ yields:

$$h_c = \sqrt{\frac{\lambda R_0}{2}}. \tag{7}$$

The sign convention for h designates whether the knife-edge lies above (positive) or below (negative) the SGP. For positive values of h, a necessary condition for significant diffraction loss, and thus for degraded positioning performance, is $h > h_c$. Given that $h_c \propto \sqrt{R_0}$, the critical height grows with the receiver-wall distance d. Consequently, the relative obstacle height h/h_c typically decreases with distance, leading to a reduction in diffraction effects.

In this work, results using real measurements are shown in Sect. Results. Controlled experiments were conducted with a real metallic movable wall of height 0.8 m at different horizontal (shortest) distances between 1 and 3 m, in steps of 0.5 m. The results confirm the values shown in Table 1, which is discussed further in Sect. Correlation and comparative analysis of residuals.

Impact of diffraction on PPP processing

PPP processing relies on the use of accurate models for various GNSS error sources. These include satellite clocks, orbits, ionosphere (using the ionosphere free combination). Most of the tropospheric (dry) delay is also well handled by established models. This information is used by the processing filter for parameter estimation. The parameters that are either unknown, or not known well, are the ones to be estimated. These are receiver positions, receiver clocks, zenith tropospheric delay corrections, and phase ambiguities. During the processing, these parameters are adjusted until the difference between the observed and the calculated phase is minimized for all satellites simultaneously. This works perfectly in a less noisy, low multipath environment with no diffraction.

However, when an obstruction, such as a metallic wall, is placed in the vicinity of the antenna, it introduces an unmodeled satellite-specific phase bias that varies with time. The extra unaccounted phase delay introduced by the diffraction at the wall then appears in the residuals, but could also be absorbed to some extent in the estimated parameters. The magnitude of the diffraction bias is larger when the wall is closer and decreases as the wall moves away, as is shown by the computations in Table 1. A larger diffraction bias means a larger miscalculation that the adjustment process must incorrectly assign to the residuals and the other estimated parameters. Thus, this leads to larger errors in many cases for the estimates of position and the zenith total delays (ZTD), a part from showing up in the residuals. This manifests as more noise and drifts in the time series, leading to a higher RMS (or standard deviation). In short, the PPP adjustment process distributes any unmodeled systematic error, in this case diffraction effects, across the estimated parameters. The closer the wall, the larger the error, and the more severely the solution is distorted.

Moreover, at higher latitudes, the errors are more pronounced in the north and up components of the position estimates. This is due to the asymmetry of the satellite constellation as viewed from the high-latitude location, affecting the dilution of precision.

Low elevation satellites provide important data for estimating ZTD. The diffraction bias due to the wall on such satellite signals are therefore interpreted as an error in the tropospheric model. The adjustment process thus erroneously adjusts the ZTD estimate to make the phase measurements from this satellite match. Since the up component of the position estimate is tightly coupled to the ZTD estimate, this also directly injects errors into height estimates. The erroneous results from PPP processing for different wall distances are shown in Sect. Diffraction impact on PPP position estimates.

Isolating diffraction effects in carrier phase residuals

As is explained in Dutta et al. (2026), the PPP technique relying on an ionosphere-free (L_3) combination of dual-frequency measurements, can introduce noise and may not be the optimal method for isolating carrier phase diffraction. We find that this is particularly true when the distance to the diffracting object exceeds 1.5 m at L_1 frequency.

As an alternative, the double-difference technique applied to a single frequency (preferably L_1) offers a more robust approach. For receivers in close proximity (separated by a few m), the atmospheric delays can be considered to

be identical, effectively treating the receivers as co-located. A single difference between the carrier phase observations from two such co-located receivers eliminates the satellite clock, and subsequent double differences removes the receiver clock error as shown in Dutta et al. (2026). Furthermore, given the co-location of the receivers, the tropospheric and ionospheric delays are effectively canceled.

Consequently, the double-difference analysis for co-located stations significantly simplifies the estimation problem. This method enables the use of a single-frequency observable, thereby avoiding the noise amplification inherent in the ionosphere-free combination and providing a clearer signal for isolating diffraction effects.

While comprehensive GNSS data processing software packages like BSW (Dach et al. 2015) account for global systematic errors (e.g., satellite orbits, clocks, ionospheric and tropospheric delays) quite well, they cannot automatically correct local, environment-dependent errors like diffraction. These unmodeled effects are a primary source of signal degradation. To quantify their impact, we analyze double-difference residuals from single-frequency observations between co-located stations, which allows us to attribute the residual signal to diffraction, which in this case, is affecting a single receiver. Also, as explained in Dutta et al. (2026), for minimizing hardware related biases, use of similar receiver-antenna set up is recommended for the co-located stations.

Experimental set up and methodology

Controlled environment description

A series of controlled experiments were conducted in a near-multipath-free environment at the Onsala Space Observatory, Sweden to isolate and quantify the impact of diffraction under varying obstruction geometry. The experiment site, located on an elevated cliff (see Fig. 2a), was chosen to eliminate signal obstructions from buildings or foliage, thereby ruling out other NLOS and multipath effects. To the south and west, the site overlooks the sea at a lower elevation, while landmass with sparse vegetation lies to the north, northwest, northeast, and east.

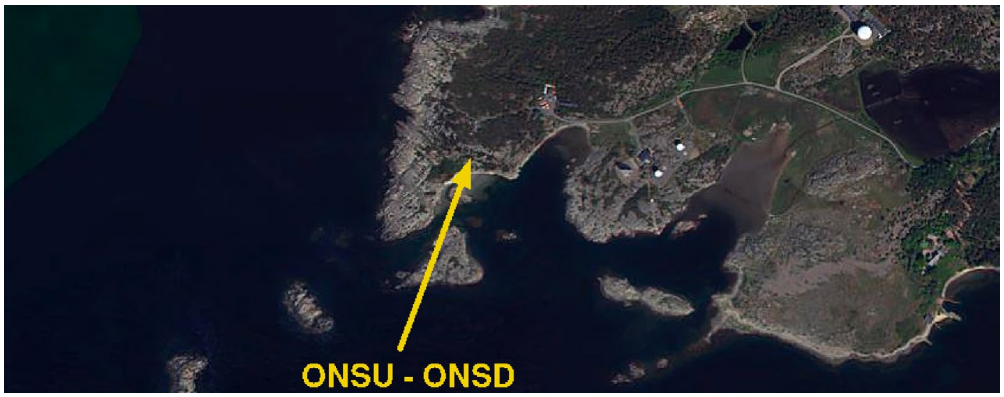
Two GNSS stations–ONSU and ONSD–were established on stable bedrock platforms, separated by a 10 m baseline. This configuration allows for analyzing diffraction impact on both Precise Point Positioning (PPP) and network-based solutions. ONSU serves as the undisturbed reference antenna, while ONSD is the disturbed antenna subjected to intentional diffraction via a movable metallic wall. The initial setup is shown in Fig. 2b

Significant care was taken during installation to minimize non-diffraction error sources. The height difference between ONSU and ONSD is less than 1 cm, ensuring tropospheric error does not obscure decimeter- to centimeter-level diffraction signatures. At a 10 m baseline, ionospheric delays are nearly identical between stations. Both stations use identical hardware: Septentrio PolaRx5 receivers and Leica AR20 choke-ring antennas, with individual robotic calibration files applied during processing. This eliminates equipment-related biases in the network solution. The receivers operate in a master–slave clock configuration to maintain a controlled clock error. Cable lengths and types are matched between antennas and receivers.

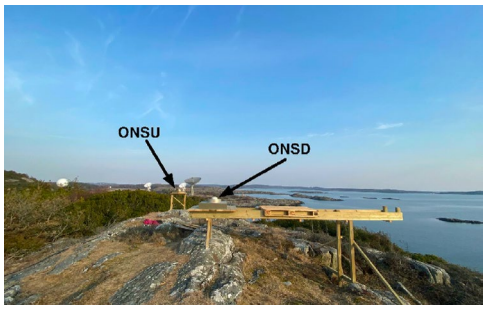
The stations first operated undisturbed, i.e. without any obstructive wall, to determine accurate reference coordinates. Subsequently, a 1 m × 1 m, 2.5 mm-thick stainless steel wall was mounted on a sturdy wooden rail near ONSD (Fig. 2c). The wall's top edge was positioned 80.6 cm above the ONSD antenna phase center. The wooden rail, oriented at an azimuth of 199° relative to ONSD, points southward–a direction with high satellite density at the site's latitude of 57°N–to maximize signal obstruction. To further suppress multipath, the side of the wall facing ONSD was clad with Eccosorb™[1] as is seen from Fig. 2f. The robust mount ensured stability even under high wind conditions, preventing vibrations that could introduce unintended signal variations.

Both receivers employed Septentrio's onboard multipath mitigation (APME+), which was active during the experiment period. The PolaRx5 is a modern geodetic reference receiver widely used in networks such as SWEPOS, and the LEICA AR20 is a well-established choke-ring antenna. For day 100 of 2026 the PolaRx5 and variants have a share of about 47 % of all the receivers committed to the IGS (CDDIS 2026). The combination is thus well suited for this experiment, though the choice was partly governed by hardware availability. While APME+ may partially attenuate multipath-induced phase errors, the suppression of unwanted signals in this study relies primarily on the experimental design, the wooden mounting structure and Eccosorb™ cladding, rather than on receiver capabilities. Diffraction, being a LOS bending phenomenon rather than a reflection, is not usually mitigated by such algorithms. The APME+ feature was tested during the experiment. For the 1 m setup with Eccosorb, the receiver-applied carrier-phase multipath corrections reaching a maximum of approximately 200 mrad at the disturbed station, and slightly less at the undisturbed station. The extent to which these corrections interact with diffracted signals remains to be investigated and can be addressed in a future work. However,

[1] A microwave-absorbing foam from Laird Technologies.



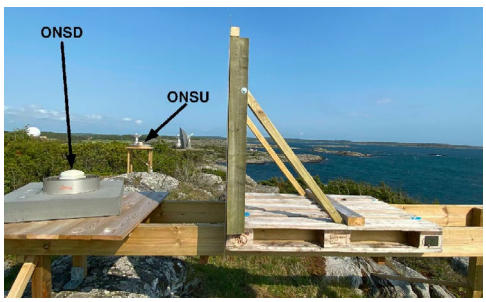
(a) Geographic location of the ONSU–ONSD installation at the Onsala Space Observatory



(b) View of the installation from west



(e) View of the installation from the north



(c) Installation with the wall



(d) Metallic box housing the receivers



(f) Wall with Eccosorb™cladding

Fig. 2 Experimental setup showing **a** the geographical location of ONSD and ONSU at the Onsala Space Observatory, **b** the ONSD–ONSU installation as seen from the west, **c** the ONSU–ONSD installation with the wall near ONSD as seen from the West, **d** metallic box housing the receivers, **e** the ONSU–ONSD installation as seen from the north and **f** Eccosorb^{TM} wrapped around the metallic wall to suppress reflections

Table 2 Table showing how the metallic wall obstruction was moved with respect to the fixed antenna ONSD

Distance (m)	Day of year 2025	Eccosorb^{TM}	Number of days
No wall	104–160	–	56
1	171–185	Yes	14
1.5	185–203	Yes	18
2	203–224	Yes	21
2.5	224–237	Yes	13
3	237–245	Yes	8
1	251–258	No	8

for this work the controlled absorber-on (DOY 171–185) and absorber-off (DOY 251–258) comparison confirms that residual multipath is negligible in the Eccosorb^{TM} configuration (see Table 5).

Data collection procedure

Data was collected at a 1 Hz sampling rate over several months from March to August 2025. A timeline of the experimental phases is provided in Table 2. Initially, both stations operated without obstruction for 56 days. This undisturbed period established precise reference positions for each station, which were used for position fixing in the network solution (detailed in Sect. Data processing methodology). The data from the initial phase also characterized the open-sky signal conditions for ONSU and ONSD, serving as a baseline for subsequent signal-to-noise ratio (SNR) analysis.

On day of year (DOY) 171, the Eccosorb^{TM} clad metallic wall (Fig. 2f) was installed near the ONSD antenna. The wall was then systematically repositioned to different distances from ONSD, as summarized in Table 2. Each position creates a distinct diffraction geometry, the effects of which are analyzed in Sect. Results.

Data processing methodology

The original data of ONSU and ONSD in RINEX format (IGS 2018) were analyzed using the post-processing softwares GipsyX and BSW. Data of the GPS and Galileo constellations were used for the PPP processing using GipsyX and the network processing using BSW. GipsyX PPP processing uses L_3 combinations of GPS L1W and L2W data and Galileo L1C and L5Q data. Single frequency data of GPS (L1C) and Galileo (L1C) were used for double difference processing using BSW.

The procedure for obtaining the BSW residuals was similar to that used in Dutta et al. (2026). Single frequency double difference network processing between co-located stations was used. Position estimation was avoided and therefore carefully monitored positions over long periods of time were used to fix the coordinates of the co-located ONSU–ONSD stations. In order to fix the coordinates of the two stations, 56 days data obtained during DOY 104–160 were used for PPP processing using GipsyX. Daily position estimates using an elevation cutoff of 10^o were averaged over this period of time to obtain final positions. These final positions were fixed for use in network processing using BSW to obtain the network residuals shown in Sect. Residuals from ONSD to ONSU network processing. Details of the data processing strategies can be seen in Table 3. In the BSW network processing, receiver clocks cancel out as explained in Sect. Isolating diffraction effects in carrier phase residuals. Estimation of atmospheric parameters were

Table 3 Summary of GNSS data processing strategies employed for PPP and double-difference (DD) network analysis

Processing aspect	PPP (GipsyX)	Double-difference network (BSW)
Software	GipsyX (Bertiger et al. 2020)	Bernese GNSS software (Dach et al. 2015)
Constellations	GPS + Galileo	GPS + Galileo
Observable	Ionosphere-free linear combination (L_3)	Single frequency (L_1)
Sampling interval	5 min	30 s
Elevation cutoff	3°	3°
Stations processed	ONSD (disturbed) and ONSU (reference)	ONSD (disturbed) and ONSU (reference)
Baseline length	–	10 m
Station coordinates	Estimated	Fixed to long-term PPP mean
Receiver clock	Estimated	Eliminated by double differencing
Satellite orbits and clocks	JPL final products	CODE final products
Ionosphere	Eliminated by L_3 combination	Canceled by short baseline; not estimated
Troposphere	Estimated (ZTD + gradients)	Canceled by short baseline; not estimated
Phase ambiguities	Estimated as float	Estimated as float/ integer
Antenna calibration	Individual robot calibrations	Individual robot calibrations
Reference frame	IGS20	IGS20
Primary output	5 min position estimates and residuals	Double-difference carrier-phase residuals

inhibited as the stations used are co-located. The attempt to avoid estimation of multiple parameters ensured that there were fewer estimated parameters that can absorb errors which are caused due to local unmodeled effects. In this paper all the residual plots show the first residuals of GPSEST of BSW. At this processing step, the ambiguities obtained are float values. However, after the complete ambiguity resolution processing with BSW, these are converted to integer estimates. Sect. Diffraction effects on ambiguity resolution for the ONSD–ONSU baseline presents the statistics of degraded integer ambiguity resolution efficiency due to diffraction.

In order to show the impact of diffraction on PPP processing, 5 min position estimates using an elevation cutoff of 3^o were also computed using GipsyX. These position estimates and their residuals are discussed in detail in Sect. Diffraction impact on PPP position estimates. The standard deviation (σ) value is taken as an indicator for comparing the different subplots for position estimates. To quantify the precision of the estimated σ and mean biases, 95 % confidence intervals were computed using a block-bootstrap (2000 resamples, 1-hour blocks) that preserves the temporal correlation of the PPP position time series. Significance of a bias is reported when the corresponding confidence interval excludes zero.

Results

Diffraction impact on PPP position estimates

In this section the results obtained from PPP processing using GPS and Galileo measurements at an elevation cutoff of 3^o are shown. The estimations were made using GipsyX PPP software at 5 minute intervals for the data obtained from ONSD during 24 March to 2 September 2025. Figure 3 shows the color plot of the PPP residuals plotted on an azimuth elevation grid. The values of azimuth and elevation are in degrees, while the color scale indicates values of the obtained residuals in m. Figure 3a shows the plot of residuals obtained during the undisturbed period DOY 111 – 160 i.e. before the wall was introduced. From the color scale one can see that there are no large residuals in this plot. Figure 3b shows the plot of residuals obtained during the period DOY 171 – 184 when the wall was installed and placed at 1 m distance from ONSD. The large residuals (plotted in dark red) clearly indicate the presence of wall in the neighborhood of azimuth 200^o. This is also the location of the wall as indicated by the black window in Fig. 3b. The wall is covered by Eccosorb^{TM} and therefore there is no reflection from the surface of the wall from direct line of sight signals from the north. The availability of signal / measurements inside the wall window even at low elevations is an indicator of signal bending. This means that all GPS and Galileo satellites at these elevations are still visible to the receiver, though there is no direct line of sight. Since the signals traverse a longer path length due to bending on the top edge of the wall, therefore the values of the residuals are always positive.

One can also see that the color inside the wall window changes from smaller to larger values as elevation decreases which is expected and verified already from the computations in Sect. Physics of diffraction and Table 1. These residuals have a maximum value of 9 cm in the azimuth of interest. This is, however, smaller than the computed diffraction error level shown in the Table 1. As already explained, the wavelength dependent diffraction error is not optimally reflected in the PPP estimates due to the L_3 combination. But this also points to the fact that the error is absorbed by other parameters that were estimated simultaneously. In this case this is clearly seen in the position estimates.

Time series of the differential changes with respect to mean position estimates for ONSD in the east, north and up direction, respectively are shown in Figs. 4, 5 and 6. Each of these figures have 6 subplots that correspond to case-1 with no wall and cases 2 to 6 with the wall moved from 1 to 3 m, as indicated by text boxes on the top left of each subplot. The y axis units are m. The σ value is taken as an indicator for comparing the different subplots. The σ for the time series of each case is shown in the text box to the bottom right of each subplot. For these figures, the mean of

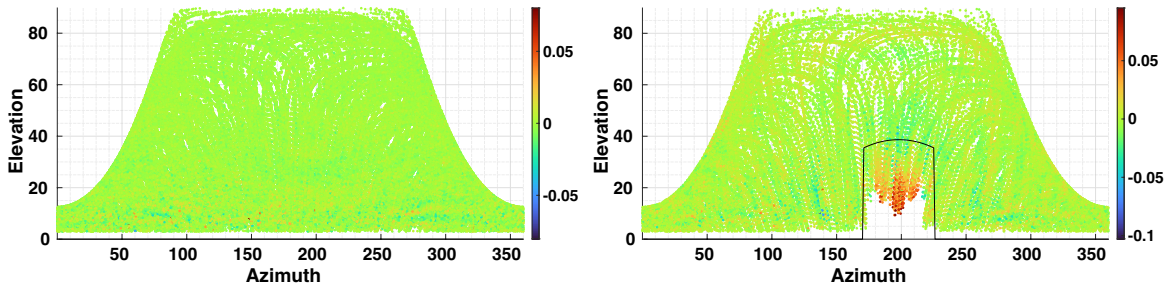


Fig. 3 GipsyX PPP residuals using GE data for ONSD **a** with no wall, **b** with wall at 1 m distance. The color bar shows the color scale for the residual values in m

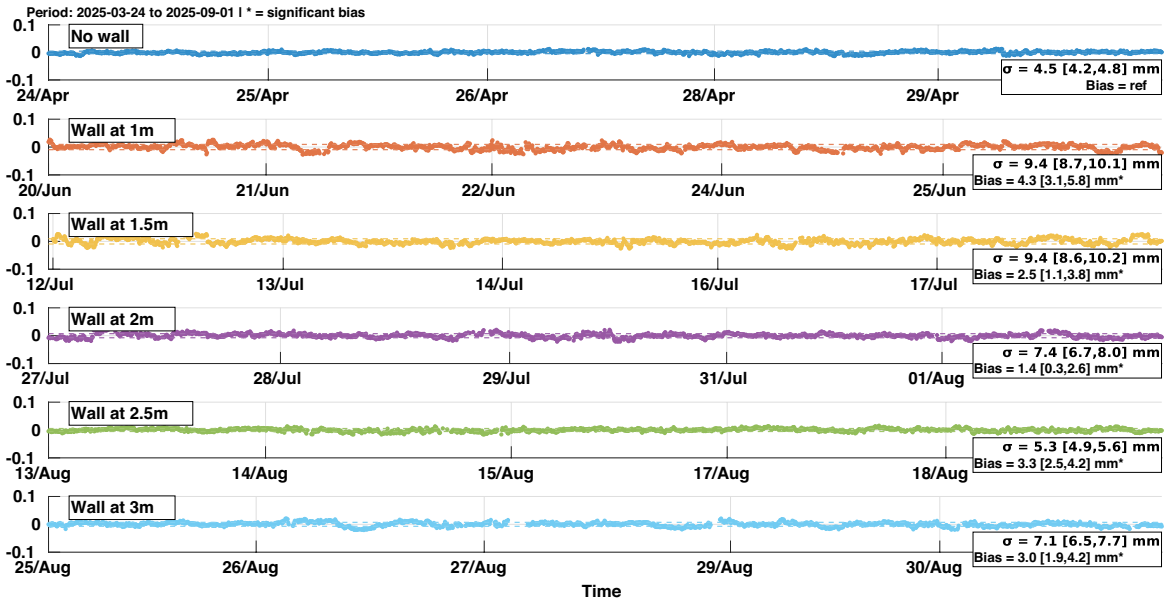


Fig. 4 East direction time series of position estimates for ONSD after removing the mean of each wall-distance period. The vertical axis shows values in m. Text boxes on the top left of each subplot indicate the wall distance. The σ and bias with 95% bootstrap confidence intervals in brackets are shown in the text box at the bottom right of each subplot. Biases are computed relative to the no-wall reference period (top panel); a star ($*$) marks biases that are significant since their confidence interval excludes zero. While σ changes with wall distance, east coordinates are least affected

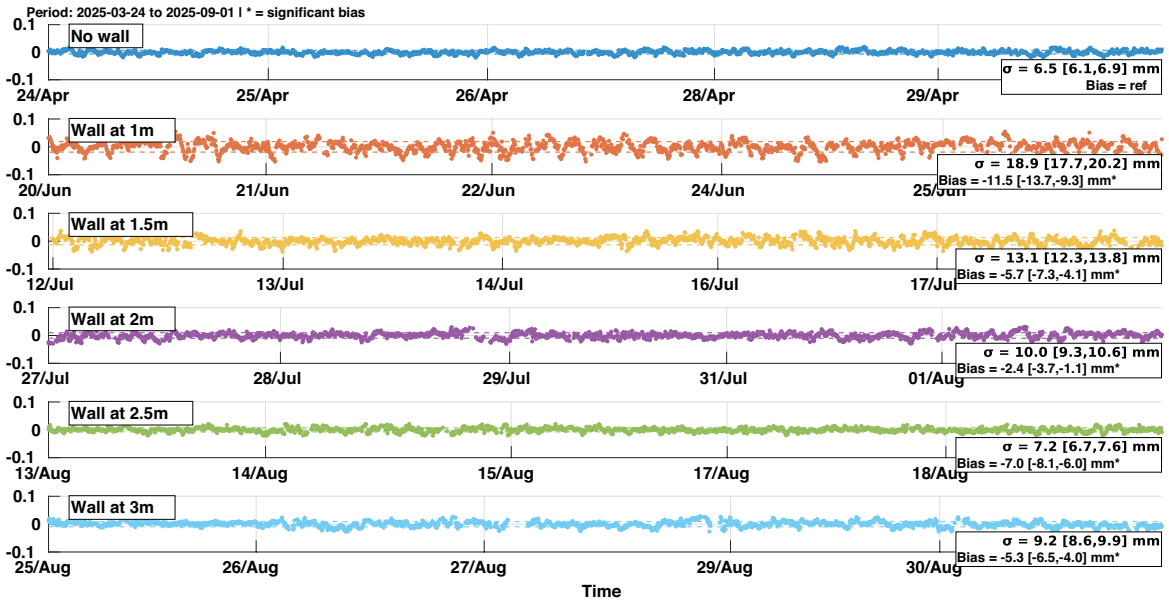


Fig. 5 North direction time series of position estimates for ONSD after removing the mean of each wall-distance period. The vertical axis shows values in m. Text boxes on the top left of each subplot indicate the wall distance. The σ and bias with 95% bootstrap confidence intervals in brackets are shown in the text box at the bottom right of each subplot. Biases are computed relative to the no-wall reference period (top panel); a star ($*$) marks biases whose confidence interval excludes zero. The different distances of the wall have a large impact on the north coordinates as reflected in the changing σ values

each 8 days period was first subtracted to separate systematic offsets from the intrinsic scatter; the systematic biases are further analyzed in Sect. Resolution of the 3 m anomaly: noise and not diffraction. For each of the different wall distances, 8 days of continuous data from each period shown in Table 2 are used for the time series plots and the calculation of the σ values. The site was chosen for its unobstructed sky view, but its remoteness and the logistical demands of repositioning the wall mount resulted in datasets of unequal duration. To enable a fair comparison, all datasets were

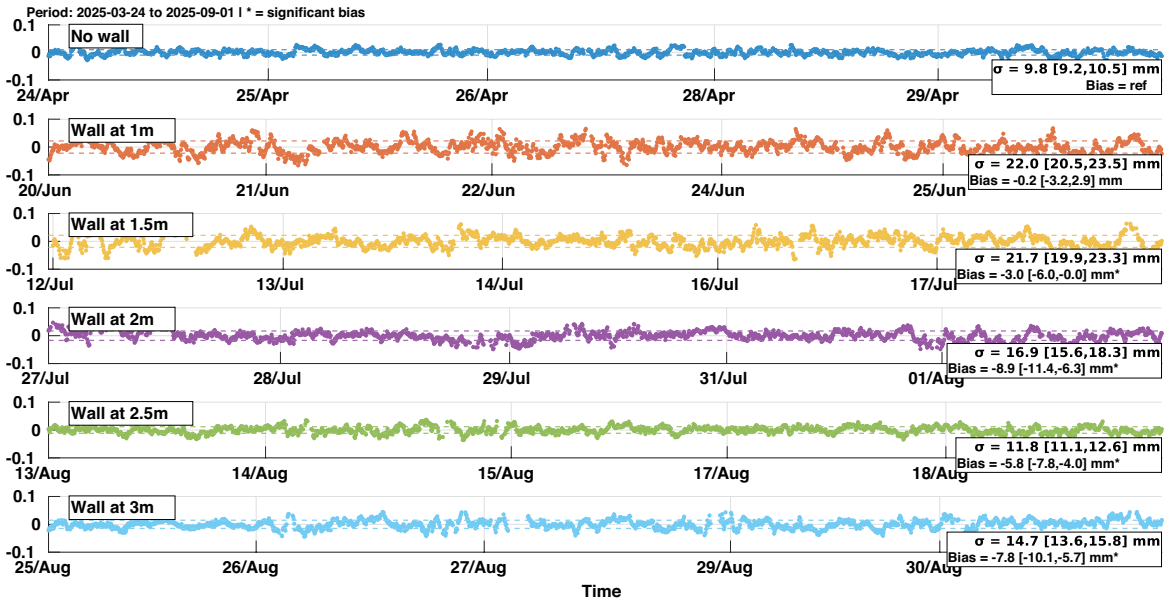


Fig. 6 Up direction time series of position estimates for ONSD after removing the mean of each wall-distance period. The vertical axis shows values in m. Text boxes on the top left of each subplot indicate the wall distance. The σ and bias with 95% bootstrap confidence intervals in brackets are shown in the text box at the bottom right of each subplot. Biases are computed relative to the no-wall reference period (top panel); a star ($*$) marks biases whose confidence interval excludes zero. The up component in the position estimates are most affected due to the changing distances of the wall and this is reflected in the changing σ values

standardized to a minimum common length of 8 days–the shortest continuous subset available. This window exceeds the 3 sidereal days needed to capture GPS multipath repeatability, while providing sufficient averaging to suppress random variability. Although the GNSS constellation evolves slowly over time, the stationary multipath environment dominates the signal of interest over these durations. Using consistent 8-day subsets therefore isolates the wall-distance effect without introducing any meaningful sensitivity to the chosen span.

As expected, for cases with the wall, consistent phase biases on a subset of blocked satellites will translate into biased position estimates. However, as is already explained, in Sect. Impact of diffraction on PPP processing, the north and the up components are the most affected by the metallic wall. The change in σ for the east component from a 'no wall' to a 'wall at 1 m' case is a few millimeter. But for the north and up component this change is in centimeter. As predicted by Dutta et al. (2026) with simulations, the σ increases by approximately a factor of two or more in all the three components for 1 m wall distance as compared to the 'no wall' case. As is expected, the σ is lowest for the baseline case with no wall. This increases to maximum when the wall is closest at 1 m and reduces as the distances to the wall increases.

A low-elevation satellite's line-of-sight path has a long slant distance through the atmosphere. Therefore including low elevation data is recommended for estimating the tropospheric zenith delay. The diffracting wall primarily blocks low-elevation satellites in the South. The PPP adjustment process, receiving erroneous phase data from these low-elevation satellites, makes errors in estimating the tropospheric delay. An error in tropospheric delay maps almost directly into an error in the up component.

This coupling typically makes the up component the most affected (Fig. 6). As seen from Fig. 7, at 1 m, the North σ reached 18.9 mm with a confidence interval bound of [17.7, 20.1] mm. This is a 2.9 fold increase over the no wall reference while a systematic southward bias of -11.5 $[-13.7, -9.3]$ mm was observed. Significance of a bias (or σ change) is reported when the corresponding confidence interval excludes zero (or a ratio of 1). Both effects were statistically significant.

It is seen that the σ is lowest when the wall is at 2.5 m distance. After this, the σ increases slightly (by about 2 to 4 mm) for all the three components. This is because the experiment likely reaches a cross-over point. At close distances between 1 and 2 m, the diffraction effect from the wall is the dominant source of error. However, at a certain distance (around $2.5 - 3$ m), the diffraction error becomes comparable to, and then smaller than, the background noise floor. This is analyzed in detail in the next section.

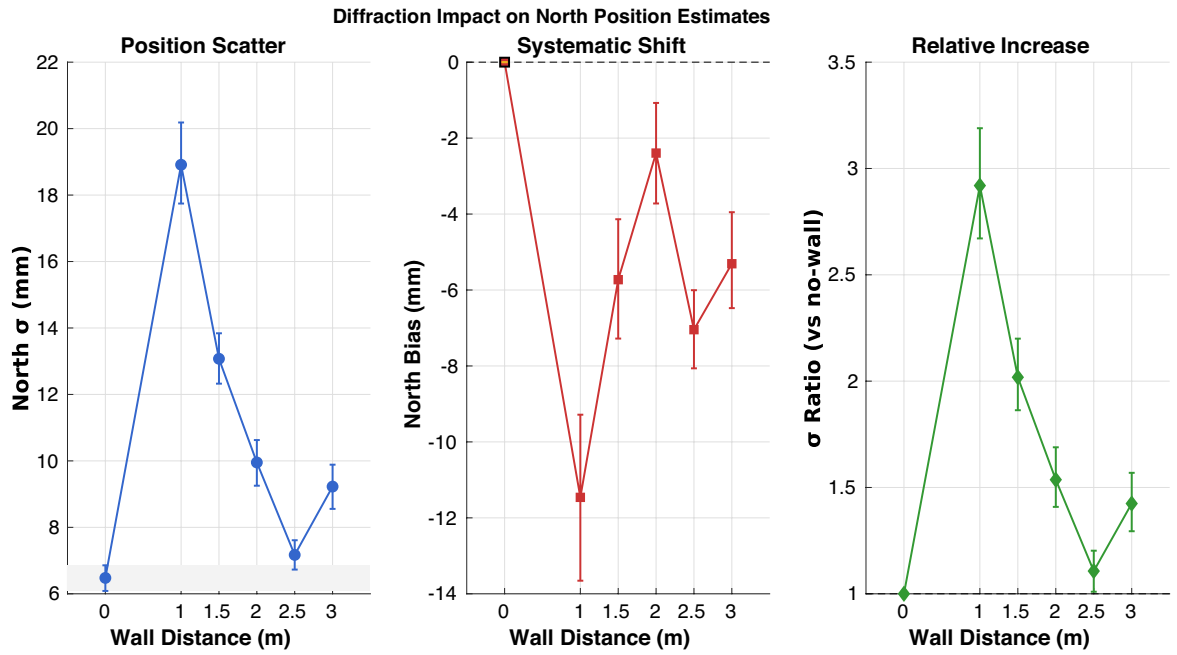


Fig. 7 Diffraction impact on the PPP (north) position estimates of ONSD. Figure shows the position scatter, systematic shift and the relative increase of σ with respect to the no wall case. The error bars show the 95 % confidence intervals generated using block-bootstrap

Resolution of the 3 m anomaly: noise and not diffraction

It is suspected that the rise in σ between the 2.5 and 3 m distance cases is not due to diffraction, but is due to an increased noise floor. In order to understand this in detail, the baseline between ONSU and ONSD was computed using the GipsyX coordinates and analyzed. The analysis in this section is done primarily for the north and the up components since these are the most affected as discussed in the previous section. As explained earlier, this helps in canceling commons errors between the two stations. It is to be noted that ONSU is an undisturbed reference station with no obstructions or disturbances in it's vicinity and is located at a baseline distance of 10 m, while ONSD was disturbed by 6 different obstruction cases, as seen in Figs. 4, 5 and 6. A 'no wall' case was followed by 5 different cases for different distances of the wall.

A static bias analysis was conducted for each of the six experimental configurations by computing the median baseline vector across all epochs from the corresponding eight-day observation periods. This median baseline serves as a reference baseline vector $B_{ref}(d)$ for each wall distance d. The static bias induced by the wall was calculated as the difference between $B_{ref}(d)$ for a given wall distance and B_{ref} for the no-wall case. The static north bias shows a monotonic decrease in magnitude from -8.62 $[-10.86, -6.12]$[2] mm at 1 m wall distance to -1.79 $[-2.35, -1.33]$ mm at 2.5 m and -1.26 $[-1.86, -0.67]$ mm at 3 m, confirming the expected reduction in systematic diffraction effects with increasing wall distance.

To characterize measurement precision while mitigating the influence of outliers, robust standard deviations were computed as IQR/1.349, where IQR represents the inter-quartile range of the central 50% of data. For a normal distribution, IQR = 1.349 σ, making this conversion to equivalent standard deviation units appropriate. However, contrary to the decreasing systematic bias, this robust standard deviation shows a 10% increase from 5.01 mm at 2.5 m to 5.51 mm at 3 m, indicating degraded precision despite reduced systematic effects.

To separate repeatable diffraction patterns from random noise, the static bias was removed from the baseline coordinates to obtain residuals. These residuals were aligned by sidereal time and stacked across the eight observation days, exploiting the sidereal repeatability of GPS satellite geometry. This approach assumes that over an eight-day period, the sidereal repeatability of GPS satellites primarily constitutes the diffraction error, creating a repeatable pattern that distinguishes it from random noise. It should be noted that the contribution of Galileo satellites in the combined GE

[2] The numbers within parenthesis report the confidence intervals. To quantify the reliability of the estimated biases, 95% block-bootstrap confidence intervals were computed for the static baseline offsets (2000 resamples, 60-minute blocks).

Table 4 Quantitative analysis of the 3 m positioning anomaly

Error type	North component			Up component		
	2.5 m (mm)	3 m (mm)	Change (%)	2.5 m (mm)	3 m (mm)	Change (%)
Static bias (magnitude)	1.67	1.26	↓25	3.78	2.62	↓31
Repeatable signal σ	3.01	2.86	↓5	4.18	5.28	↑26
Random noise	5.27	6.13	↑16	7.73	9.09	↑18

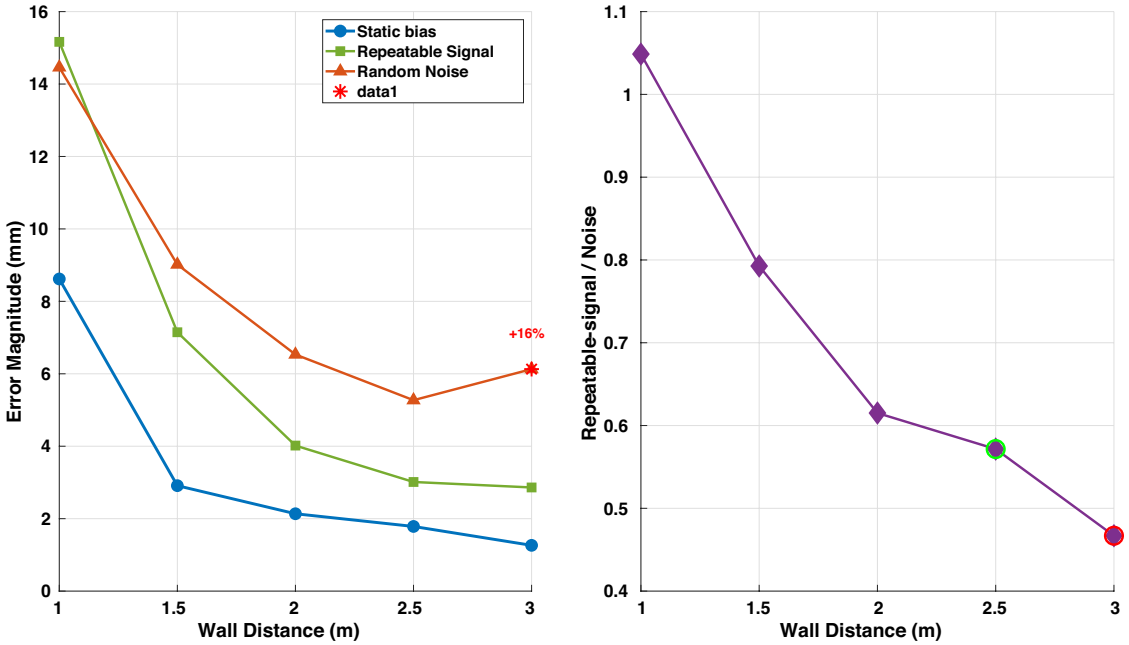


Fig. 8 Comparative plot of error magnitudes derived from GipsyX position estimates for the north component with changes in wall distances. Left: Comparison of the change of repeatable signal versus random noise, Right: Changes in ratio of repeatable-signal error to noise

solution cannot be considered in this sidereal analysis due to their different orbital characteristics.

The original 5-minute position estimates were linearly interpolated to achieve 1-minute sampling, necessary to accommodate the approximately 4-minute daily sidereal shift when stacking data. While this interpolation introduces some uncertainties, it provides an initial straightforward method for isolating non-repeatable noise, with further methodological variants to be explored in future work.

For each sidereal time bin, a median stack value was computed, representing the repeatable component at each time step. The σ of this component quantifies amplitude variations of the repeatable signal. For the north component, this decreases from 15.16 mm at 1 m to 2.86 mm at 3 m. Subtracting this repeatable signal from the residuals yields the non-repeatable noise component.

Analysis of these components reveals a critical distinction: while the repeatable signal decreases from 3.01 mm[3] at 2.5 m to 2.86 mm at 3 m, random noise increases by 16% from 5.27 to 6.13 mm, as shown in Table 4 and Fig. 8. Figure 8b also plots a ratio of repeatable signal error to random noise which shows a monotonic decrease with increasing wall distance. This demonstrates that at the 3 m distance, diffraction is no longer the dominant error source, and the anomaly observed in σ values is primarily due to increased noise.

While the analysis presented here focuses on the north component as an example, similar conclusions apply to the up component, though with some differences. For the vertical component, the repeatable signal shows a 26% increase at 3 m (4.18–5.28 mm), likely because low-elevation satellites (down to 3°) are visible and are affected by the wall at 3 m, directly impacting the up component estimate. Despite this difference, noise remains the predominant component, increasing by 18% from 7.73 to 9.09 mm.

In a PPP processing, the atmospheric conditions play a very important role. Because the six experimental configurations span different calendar periods, we verified that seasonal atmospheric variability does not primarily affect the conclusions of the wall-distance comparison. The ONSU–ONSD baseline cancels common-mode tropospheric and ionospheric delays. The non-repeatable scatter during the

[3] Formal bootstrap uncertainties for the repeatable signal and the non-repeatable noise are not reported here because the sidereal stacking introduces variable bin occupancy that would require a specialized resampling scheme. This is left to a dedicated future study.

no-wall period therefore defines a combined (atmospheric and process) noise floor of 4.3 mm (North) and 6.4 mm (Up). The repeatable diffraction signal at 1 m (15.2 mm) exceeds this floor by a factor of three and decreases monotonically with wall distance. This behavior is inconsistent with randomly varying atmospheric conditions, confirming that the reported trends are driven mainly by diffraction, not weather.

The comprehensive error decomposition explained in this section reveals that the apparent 3 m wall distance anomaly results from larger random noise rather than enhanced diffraction effects. Systematic diffraction continues to decrease with wall distance, but the positioning enters a noise-dominated regime at 3 m where increased random errors elevate the total σ.

DOP metrics under diffractive conditions

As noted by Dutta et al. (2026), low Dilution of Precision (DOP) values can occur simultaneously with large, systematic errors in obstructed environments. This is demonstrated by the consistently low Position DOP (PDOP) values – nearly equal to 1 – computed for our data (Fig. 9). Such values reflect geometric satellite distribution but remain blind to the obstruction, making DOP an insufficient sole indicator of positioning quality.

Residuals from ONSD – ONSU network processing

In this section the results obtained from network processing using GPS and Galileo measurements at an elevation cutoff of 3° are shown. The estimations were made using BSW at 30 second intervals for the data obtained from ONSD and ONSU during 24 March to 2 September 2025. The position fixing and the data processing methodology is explained in Sect. Data processing methodology.

Figure 10 shows the single frequency (L1C) residuals obtained using BSW for different wall distances of 1–3 m. The black window in each plot indicates the shadow of the wall which decreases as the wall moves away. The color scale shows the value of the obtained residuals in m. When the wall is at 1 m distance, the residuals obtained have a maximum value of a few decimeter, but this reduces to a few centimeter as the wall moves away to 3 m distance. In the double difference residuals the satellite and receiver clock errors cancel out. Also, since the ONSD–ONSU stations are co-located, atmospheric errors cancel out. The residuals therefore are generated due to the unmodelled effect caused by the wall. Occurrence of multipath is ruled out with the use of Eccosorb^{TM}. However, there could be possibilities of multipath due to reflections when the wall does not have Eccosorb^{TM} and therefore Fig. 10f is included for the purpose of comparison. The wall window in Fig. 10f has much more number of data points than Fig. 10e.

Isolation of diffraction from residual multipath

To verify that the Eccosorb^{TM} cladding effectively suppresses surface reflections, we compared double-difference residuals inside the wall shadow at 1 m distance (azimuth 199 ± 27°, elevation ≤ 39°). The comparison was made for three configurations: the undisturbed period (no wall),

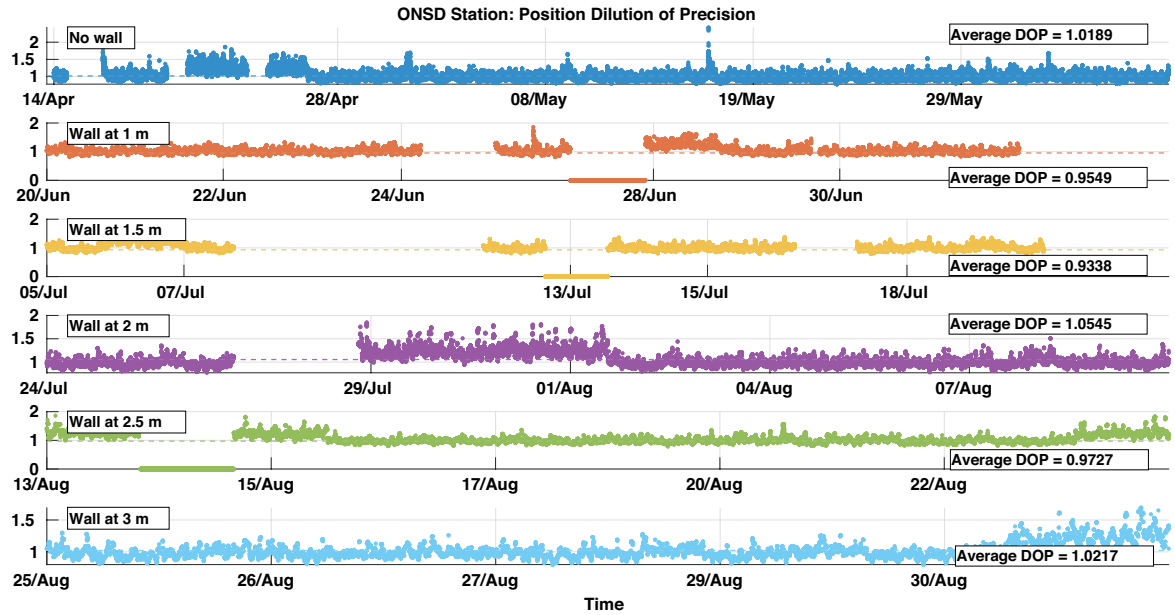
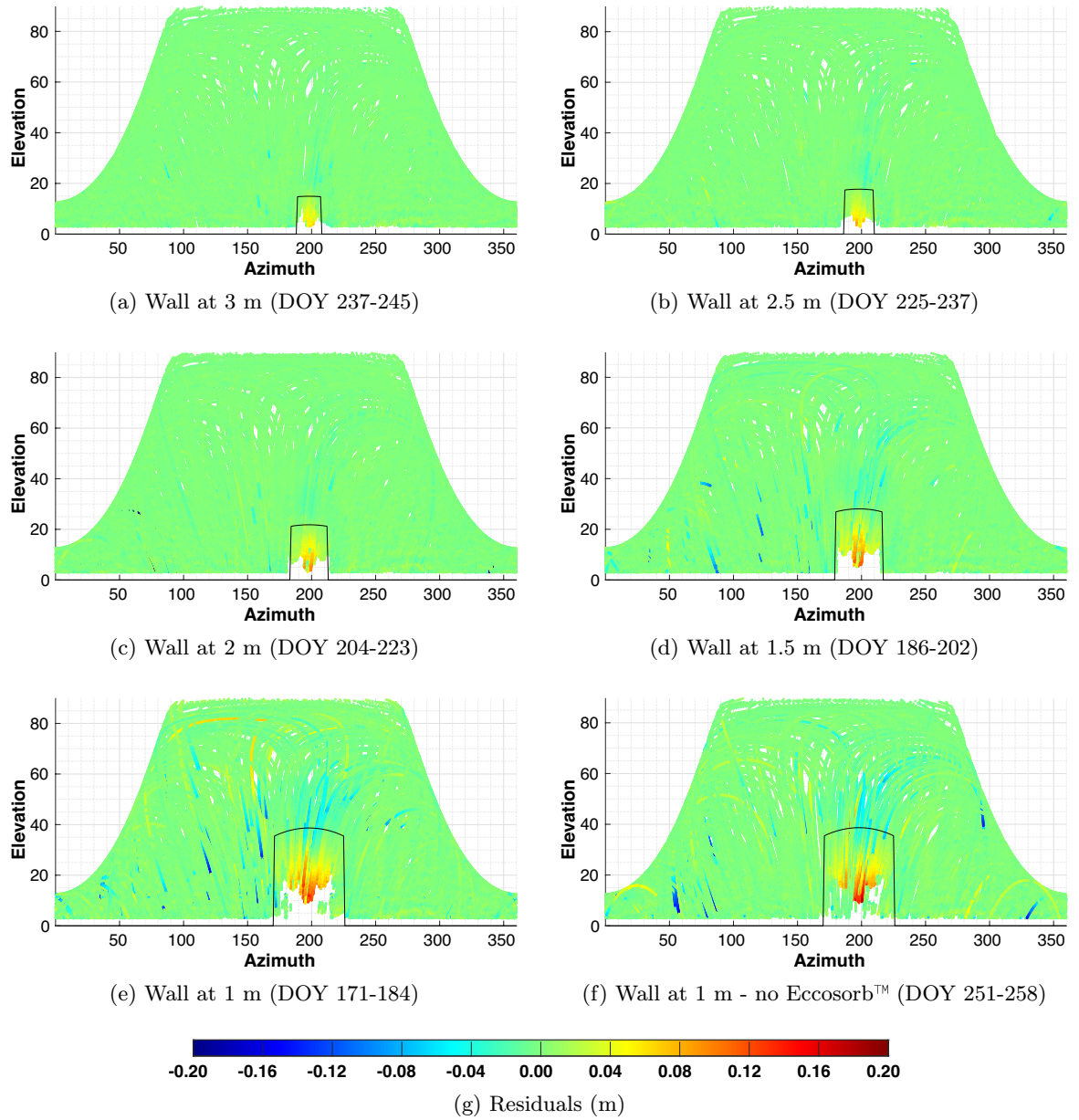


Fig. 9 PDOP computations at the ONSD station show consistent low values indicating good satellite geometry irrespective of the position of the wall



(a) Wall at 3 m (DOY 237-245)

(b) Wall at 2.5 m (DOY 225-237)

(c) Wall at 2 m (DOY 204-223)

(d) Wall at 1.5 m (DOY 186-202)

(e) Wall at 1 m (DOY 171-184)

(f) Wall at 1 m - no Eccosorb™ (DOY 251-258)

(g) Residuals (m)

Fig. 10 BSW double difference GE residuals for the ONSD–ONSU baseline for the first frequency (L1C) observable with the wall at distances of **a** 3 m **b** 2.5 m **c** 2 m **d** 1.5 m **e** 1 m **f** 1 m (without Eccosorb^{TM}) **g** colorbar showing residuals in meters. Changes in the position of the wall show clear signature of the diffraction impact on the residuals

Table 5 Separation of diffraction and multipath using double-difference residuals inside the wall shadow

Configuration	RMS (mm)	95 % CI (mm)
No wall	3.9	[3.9, 4.0]
1 m + Eccosorb^{TM}	36.8	[36.4, 37.2]
1 m (bare metal)	39.8	[39.2, 40.5]
Diffraction component	32.9	–
Multipath component	3.0	–

CIs are 95% bootstrap confidence intervals

the wall at 1 m with Eccosorb^{TM} and the wall at 1 m without Eccosorb^{TM} The RMS of the residuals was 3.9 mm without the wall, rising to 36.8 mm with the absorber-clad wall and to 39.8 mm with the bare metal wall as shown in Table 5. The increase from the background noise (32.9 mm) is attributable to diffraction, whereas the additional 3 mm caused by removing the absorber represents residual multipath. The non-overlapping confidence intervals confirm that the multipath contribution is statistically distinguishable but an order of magnitude smaller than the diffraction effect,

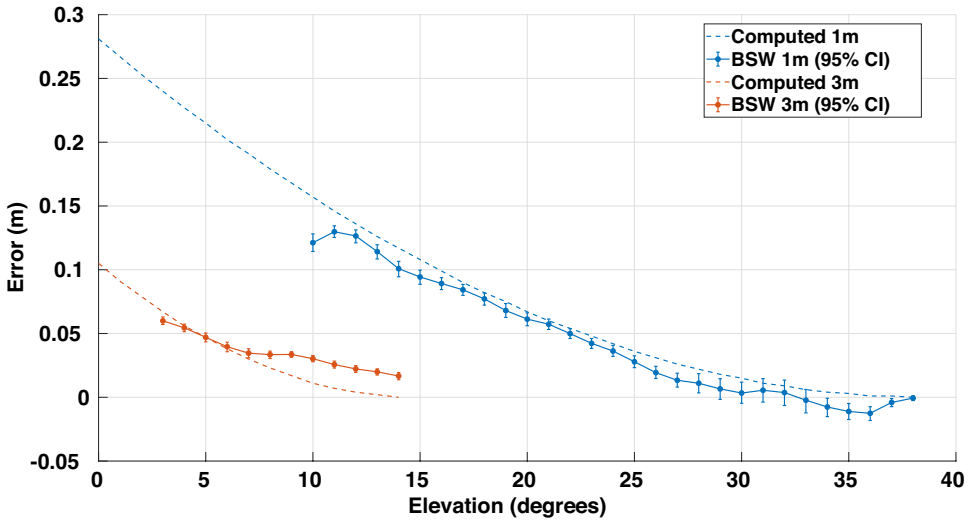


Fig. 11 Comparison of computed diffraction errors using geometry (dotted lines) with BSW obtained residuals (solid lines). Error bars show the 95% bootstrap confidence intervals for the mean double differenced residual in each elevation bin. Two different cases for the wall at 1 m (blue) and 3 m (in red) are shown. The values in the y axis are in m

validating the experimental design and isolating diffraction as the dominant error source.

Correlation and comparative analysis of residuals

Figure 11 shows a comparison between the computed values of diffraction error shown in Table 1 and BSW obtained residuals plotted in Fig. 10. For simplicity, all computations were performed for a single reference azimuth of 199° . At this azimuth, BSW residuals are grouped by satellite elevation, averaged within each elevation bin, and assigned a single representative value. These averaged residuals together with computed values are then plotted for two wall distances – 1 m and 3 m – as shown in the figure.

It is to be noted that the BSW residuals are double-differenced. This means that at each epoch, they are a function of the receiver pair (ONSU, ONSD) and two satellites with different locations in the sky. Given that ONSU serves as an undisturbed reference station, its contribution to the residuals can be considered negligible. Consequently, the dominant components of the residuals are the errors originating from the ONSD receiver and the diffracting wall. However, there are also two satellites involved. This is discussed further in Sect. Discussion.

Diffraction effects on ambiguity resolution for the ONSD – ONSU baseline

For the double-difference processing, the estimation of all other parameters including coordinates and troposphere was inhibited, to ensure that the errors are retained in the residuals. Thus, we estimated only ambiguities. We assessed the impact of diffraction on GNSS ambiguity resolution using the ONSU–ONSD baseline data. For this, BSW solution files from the unobstructed period (DOY 104–160) were compared with those from the period when the wall was placed at 1 m distance from the receiver (DOY 171–184).

Table 6 Statistics of the BSW ambiguity resolution for GPS measurements on the ONSU–ONSD baseline

Metric	Without wall	With wall (1 m)
Fix rate (%)*	98.0 ± 1.7	93.4 ± 7.0
RMS after fix (mm)*	0.43 ± 0.05	2.58 ± 0.16
Unfixed ambiguities (%)	2.6%	6.3%

* Mean ± standard deviation

As is seen from Table 6, the presence of the wall resulted in an increase in RMS from 0.43 to 2.58 mm, a reduction in the fix rate from 98.0 to 93.4%, and an increase in unfixed ambiguities from 2.6 to 6.3%. These changes also illustrated in Fig. 12, further validate that diffraction caused by a wall at 1 m distance introduces systematic errors that affect the overall quality of the post processed solution.

Modeling signal-to-noise ratio

The KED model explained in Sect. Physics of diffraction is used to model the impact of diffraction on SNR measurements obtained from the ONSD receiver. Here we extend the work done in Dutta et al. (2026) and compare the modeled SNR for different distances to the wall. Figure 13 shows the plots of SNR modeling of the S1C signal for GPS satellite G08 as an example. The analysis could be extended to other GPS satellites impacted by the wall. Two extreme cases, “wall at 3 m” (Fig. 13a) and “wall at 1 m” (Fig. 13b), have been compared with the reference “no-wall” case. Figures 13c and d depict the Fresnel-Kirchhoff parameter ν and the clearance height h (m) from Eqs. 2 to 3 for the specific receiver satellite geometry at the given epoch for wall distances of 3 m and 1 m respectively. The green curve represents the modeled "no-wall" scenario, derived from a second-order polynomial fit to SNR measurements collected

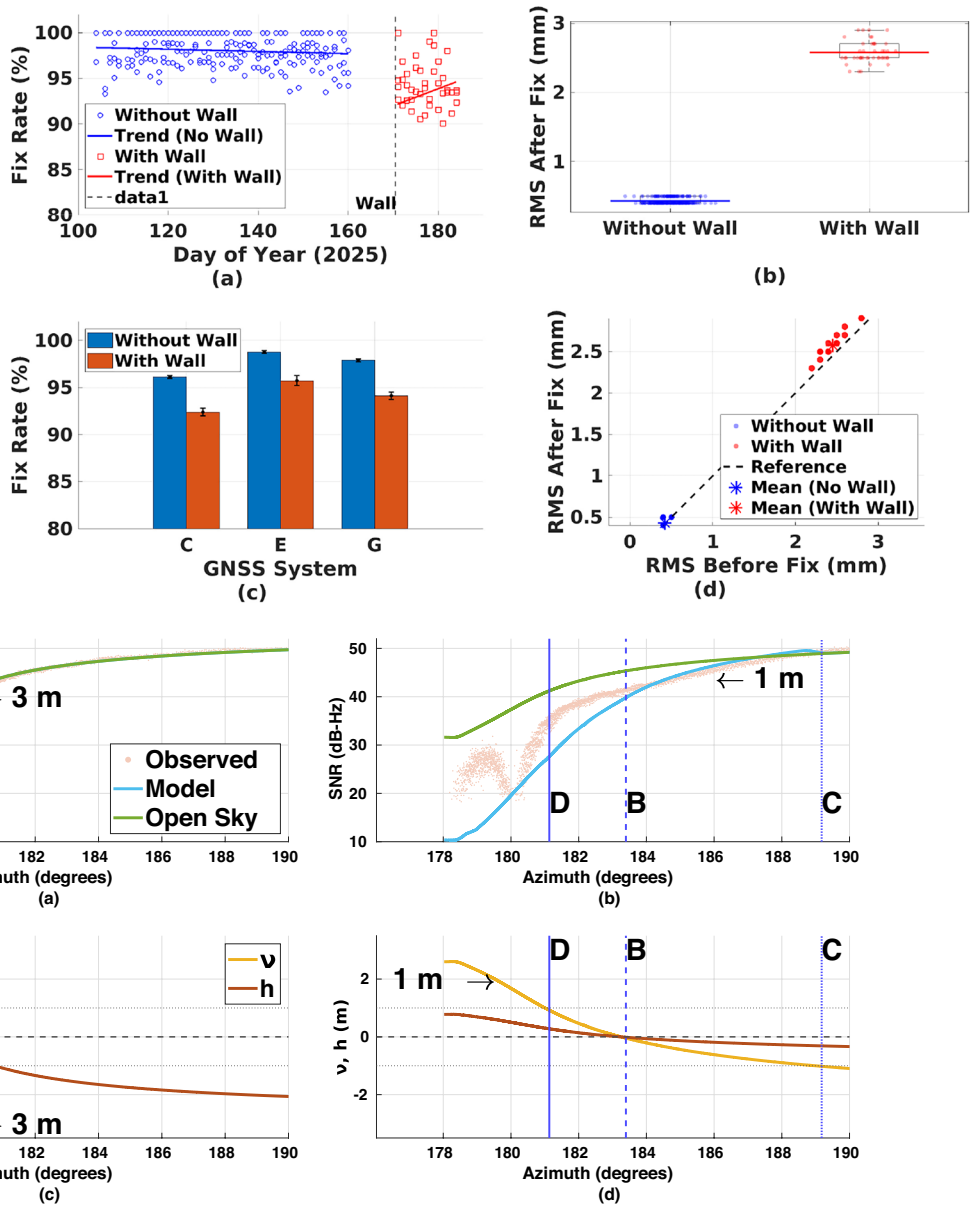


Fig. 13 SNR modeling for GPS satellite G08 using KED model. A comparison of the modeling for wall distances of 3 m (left) and 1 m (right) are presented. The reference no-loss SNR is obtained from data of the period with no wall. The vertical axis shows SNR (C/N_0 in dB-Hz) for the plots on the top and values of ν and h (m) for the plots on the bottom. The vertical lines A and B are used to represent azimuth regions where the value of h and ν are equal to zero for the 3 m and the 1 m case respectively. The vertical line C shows the point of departure of the 1 m SNR from the no-wall SNR. At this point, for the 1 m case, $\nu = -1$. The vertical line D for the 1 m case, shows the point when $\nu = 1$

during the 56-day undisturbed period (DOY 104–160; see Table 2). To the "no-wall" SNR so obtained is added the knife edge loss computed using Eq. 1 and the composite signal is then plotted. The actual observed SNR is overlaid on top of the composite SNR in red.

From Fig. 13 it is seen that for the "wall at 1 m" case the observed signal strength follows the KED model closely and decays away from the "no-wall" model prediction. However, for the "wall at 3 m" case, the impact of diffraction due to the wall is smaller as discussed before. Therefore, the modeled composite SNR is quite close to the "no-wall" model. The total loss in signal strength for the 1 m case is about 30 dB-Hz which is similar to the predictions of the KED model. However, the KED model also predicts only a 5 to 10 dB-Hz loss when the wall is at 3 m. This is verified by the actual observed values and is nearly the same amount of signal strength the satellite would have lost as it decreased in elevation even in the "no-wall" scenario. Thus,

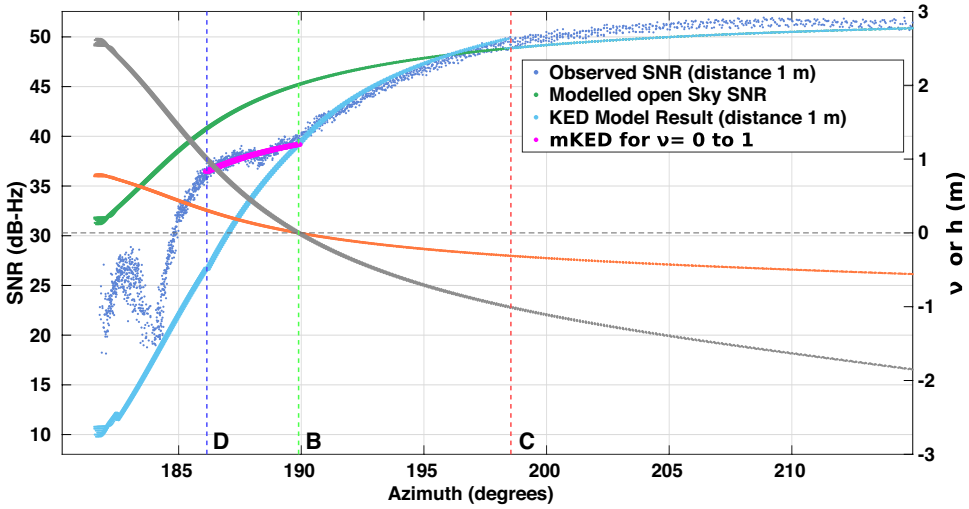


Fig. 14 SNR modeling for GPS satellite G26 using the KED model for the wall at 1 m distance case. The reference no-loss SNR is obtained from data of the period with "no-wall". The left vertical axis shows SNR (C/N_0 in dB-Hz), while the right vertical axis shows values of ν and h (m). The modified KED model (mKED) plot is shown in pink. The vertical line B is used to represent azimuth region where the value of h and ν are equal to zero. The vertical line C shows the point of departure of the observed SNR from the no-wall SNR. At this point, $\nu = -1$. The vertical line D shows the azimuth when $\nu = 1$

as pointed out earlier, diffraction is no longer a dominant source of error for the "wall at 3 m" case. Quantitatively, the root-mean-square error (RMSE) between the observed SNR and the KED model was 3.3 dB-Hz (95% bootstrap[4] confidence interval of [2.9, 3.6] dB-Hz) at 1 m but only 0.4 dB-Hz [0.36, 0.43] dB-Hz at 3 m, confirming that the far-field fit is excellent while the near-field residuals are an order of magnitude larger.

The vertical lines A and B are used to represent regions where the value of h and ν are equal to zero for the 3 m and the 1 m case respectively. The vertical line C shows the point of departure of the SNR for the 1 m case from the no-wall SNR. At this point, for the 1 m case, $\nu = -1$. As mentioned earlier, the height of the wall is constant at 0.8 m. For the case with a horizontal distance of 1 m, the value of ν obtained using Eq. 2 varies between -2.92 and $+2.58$ for values of h ranging from -0.65 to $+0.79$ m. The value of h is calculated using Eq. 3 for varying elevations of the satellite. The variations of SNR with changes in h and ν are discussed in detail in Sect. Discussion. However, it is seen that though the KED model predicts the total loss correctly, it is unable to model the signal enhancement seen in the observed values at 1 m distance immediately after line B (for values of $\nu > 0$). Specifically near the grazing incidence (line B), the mean residual (between the observed SNR and the KED model) at 1 m was 1.9 dB-Hz, whereas at 3 m the mean residual was only -0.02 dB-Hz. This reflects the KED model's systematic underestimation of SNR for the wall at 1 m case and this is noticed over all $0 < \nu < 1$ (line B to D). Thus, there is a need to modify the KED model for the near field distance of 1 m.

[4] Uncertainties were obtained via 2000-sample block bootstrap with 10-minute blocks to account for temporal correlation.

Modifying the knife-edge model

The KED model is built on basic assumptions of perfectly thin, perfectly absorbing, infinitely long edge. This is never true for real world obstructions. However, it is seen that the KED model works well for far field distances as shown in Dutta et al. (2026). But it fails to predict the apparent enhancement in signal strength noticed in 1 m distance case for values of ν ranging from 0 to 1. This signal enhancement is well demonstrated using SNR measurements from GPS satellite G26 shown in Fig. 14. The format for the plot remains similar to Fig. 13. However, for simplicity we show only the wall at 1 m distance for understanding near field effects that lead to signal enhancement for G26.

We use a least squares optimizer to model the deviation of the observed SNR from the KED model during $\nu = 0$ to 1. While the approximate KED model uses a decaying exponential to model the signal in the region $(20\log_{10}(0.5e^{-0.95\nu}))$ as shown in Eq. 1, we find that a positive value for the exponent $(20\log_{10}(0.5e^{0.1934\nu}))$ accurately models the observed SNR as shown in pink color in Fig. 14. We call it the modified KED (mKED) model. While this is observed for long term data over multiple days, it is also repeatable for other satellites. The amount of enhancement depends on the value of ν which in turn depends on the geometry of the satellite. Also, we find that, using the original KED model for the 1 m case provides a better fit to the observed values in the $-1 < \nu < 0$ region, if ν is computed using d in place of R_0 (see Eq. 2). Both the plots of original KED model shown in Figs. 13 and 14 at 1 m wall distance use d instead of R_0. Since d is always less than R_0, this indicates that the actual loss is larger than expected for such distances even before the grazing incidence. We intend to carry out further investigations to understand this behavior of the near field SNR in our future work.

Discussion

PPP processing relies on accurate information of satellite orbits and satellite clocks, as well as modeling of various GNSS error sources. Standard PPP processing softwares use models for most relevant systematic errors (Petit and Luzum 2010). However, in the presence of diffraction, which is an unmodeled error, usually, a PPP processing algorithm tries to adjust the estimated parameter values in order to achieve a minimization between the observed and the computed phases. Consequently, the estimated parameters such as receiver positions, receiver clocks, zenith tropospheric delay corrections, and/or phase ambiguities could be degraded. The results with degraded position estimates of Figs. 4, 5 and 6 are an indicator of how PPP processing can get impacted due to diffraction. Moreover as seen in these figures, at higher latitudes, the errors are more pronounced in the north and up components due to the asymmetry of the visible satellite constellation. From the position estimates it is seen that the impact is larger when the wall is close and reduces as the distances to the wall increases. Satellites at low elevation angle provide diverse geometry useful for improving the ability to estimate coordinates and tropospheric delay. However, the southern diffracting wall, in our experiment, blocks these same satellites. The use of erroneous phase signals from obstructed satellites in PPP processing introduces errors into the estimated tropospheric delay which makes the height component most vulnerable.

It should be noted that the PPP residuals are a result of L_3 processing, which is a combination of the L_1 signal and the less reliable L_2 signal. Since diffraction is a wavelength-dependent phenomenon, using an L_3 combination for quantifying diffraction impact is therefore not the best choice. One should instead look into single frequency processing, as pointed out by Dutta et al. (2026). This is possible with double differencing of co-located stations. The residuals shown in Fig. 10 are a direct indicator of the diffraction impact caused by the wall. Also, the residual plot for the wall at 1 m (Fig. 10e) case can be compared to the wall at 1 m with no Eccosorb^{TM} plot shown in Fig. 10f. The additional data points on Fig. 10f. inside the wall window show signal availability due to diffraction on the sides of the plate and also due to reflections, which have been clearly suppressed using the absorber sheet. Moreover, there is a possibility of near field effects on the plate. We note that the Septentrio APME+ multipath mitigation was active during the experiment period. While APME+ is expected to correct both code and carrier phase observations, its working principle is not known, and it remains to be investigated if it may affect diffracted signals. Future experiments with the mitigation disabled could isolate its influence on the diffracted signal, but the large difference between the absorber-on and absorber-off cases (Table 5) demonstrates that the dominant observed effect is diffraction, not multipath.

Average values of these residuals are compared with theoretical values and the plots for 1 m and 3 m case are shown for comparison in Fig. 11. Since the BSW residuals are double-differenced, at each epoch, they are a function of the receiver pair (ONSU, ONSD) and two satellites with different locations in the sky. Given that ONSU serves as an undisturbed reference station, its contribution to the residuals can be considered negligible. Consequently, the dominant components of the residuals are the errors originating from the ONSD receiver and the diffracting wall. However, there are also two satellites involved. When the wall is at 1 m distance, it casts a larger shadow on the antenna, meaning that a large number of satellites go behind the wall and their signals are then received due to diffraction. However, when these satellites descend to very low in elevation, they cannot be received any more, since the signals are too weak and vulnerable enough to be not received even with diffraction. The wall now acts as an elevation mask, completely blocking the antenna's field of view below 10^o elevation and therefore there are no residuals below this. The further away the wall is the smaller is the elevation mask. As shown in Table 1, diffraction error is positive. In a double difference satellite pair, if both satellites are behind the wall, the difference in the diffraction error contribution between them, then appears as a smaller value in the residual. It is only when one satellite (A) is above or outside the wall region and the other (B) behind the wall, that the error residual is large enough and is then attributed to satellite B alone. Therefore, the value of the residual at 1 m fluctuates, with the highest values nearly equal to that of the computed values at that elevation. The trend followed by the residuals, however, is similar to that of the computed values. It is obviously expected that the value of the residuals would be larger at lower elevations, since a larger path length is traversed by a signal from a lower elevation satellite as compared to one at a higher elevation. Also, the order of the residuals in general is similar to that of the computed values. When the wall is further away at 3 m, the values of the residuals are smaller compared to the values at 1 m and this is also expected. The wall now casts a smaller shadow on the antenna, and this means that fewer number of satellites go behind the wall and get affected by diffraction. Since the wall is further away, signals from lower elevation satellites are also visible and residuals at the 3^o elevation point this out. Thus, at lower elevations, there is a possibility of signal reception due to diffraction, but now possibly affecting only 1 satellite in most cases. Also, the impact on ambiguity resolution in the double-difference solution, shown in Fig. 12, further confirms that diffraction from a wall located 1 m away introduces systematic errors, thereby degrading the quality of the post-processed solution.

Analyzing SNR variations provides valuable physical insight into the diffraction phenomenon. We illustrate this using the L1C signal from GPS satellite G08, though the analysis can be generalized to other satellites. As shown in Fig. 1,

when the obstruction height h is positive ($h > 0$), the obstacle lies above the SGP, physically blocking the direct signal and making diffraction the dominant error source. In Fig. 13, the vertical dashed line B marks the condition $h = 0$ for the 1 m wall case, corresponding to grazing incidence. When $h < 0$, the obstruction is below the SGP; while the direct path remains unobstructed, the obstacle encroaches on the first Fresnel zone, causing SNR to begin decreasing even before line B (visible at vertical line C where h is negative). The Fresnel-Kirchhoff diffraction parameter ν (Eq. 2) further clarifies this behavior: $\nu = 0$ at $h = 0$ (line B), $\nu < 0$ when the obstruction is below the LOS, and $\nu > 0$ when it is above. For $\nu > -1$ (starting near line C), the observed SNR diverges from the no-wall reference, an effect well captured by the KED model (Eq. 1). This supports the interpretation that signal degradation can occur when an obstacle intrudes into the first Fresnel zone, even without direct blockage. For $0 < \nu < 1.6$, diffraction loss becomes significant, and the observed SNR falls to approximately 18 dB-Hz–a drop consistent with KED model predictions. However, the KED model does not fully quantify the signal degradation pattern (with a small enhancement) observed immediately after line B ($\nu > 0$), indicating a limitation of KED model in modeling near-grazing and near-field diffraction conditions. This phenomena will be studied further in our future work.

When the obstruction is moved farther away from the antenna, clearance height h and, consequently, the Fresnel-Kirchhoff diffraction parameter ν decrease. As shown in Fig. 13, at a horizontal distance of 3 m, h is negative for most of the satellite's pass, indicating that the wall no longer blocks the direct line of sight. This is true for the majority of satellites. The obstruction's shadow on the antenna and thus the overall diffraction impact is substantially reduced. This finding contrasts with the theoretical analysis of vertical diffraction error presented in Xi et al. (2025), which suggests that error magnitude increases with horizontal distance S (equivalent to parameter d in our case). Their conclusion is not empirically supported by experimental data and may implicitly assume a scenario in which obstruction height increases with distance. In practice, however, fixed-height obstacles are common.

One would rather want to stay away from a wall to a certain distance in order to avoid the impact of diffraction on the satellite signals. For the geometry tested in this work, a clearance distance of approximately 4 m provides a substantially safe margin, reducing diffraction errors to near-background levels. This also means that the elevation subtended by an obstructive environment on the antenna should not be larger than 11°. However, this 11° recommendation is subject to several constraints. It applies primarily to GNSS L_1 frequency. Lower GNSS frequencies should theoretically have larger Fresnel zones and may require more clearance, however this remains to be inspected. Moreover our experiment used a thin (compared to L_1 wavelength) metal wall that acted like a sharp edge. Thicker, rounded, or non-metallic obstacles, will change the diffraction pattern, making the 11° angle either too strict or too lenient. Different antennas, such as small survey-grade patches, may also behave differently than the Leica AR20 choke-ring antenna used here. Similar is the case for low cost receivers. It is expected that data from these devices will be more severely impacted by diffraction. The experiment took place in an open-sky cliff site with minimal impact from site-specific multipath. In cluttered environments like urban canyons, multiple diffracting edges may demand larger clearance. Finally, the 11° criterion was derived from positioning error analysis and for higher accuracy, a more conservative angle is advisable.

This clearance distance is consistent with the SNR pattern observed in Fig. 13c, at horizontal wall distance of 3 m, the ν curve is steep, transitioning rapidly from $\nu = -1$ to 0 near the grazing-incidence azimuth (dashed line A). Consequently, both the observed (red) and modeled (blue) SNR closely follow the no-wall reference (green) until grazing incidence is reached. Beyond this point, the observed SNR simply follows the reference SNR and they decline together until the satellite drops below the antenna's horizon at very low elevation (< 1°), where its signal contributes minimally to positioning.

Additionally, the proposed relationship in Xi et al. (2025)–where vertical diffraction error is larger for high elevation satellites than for low elevation ones–warrants further investigation. In typical diffraction scenarios, lower-elevation signals are generally more susceptible to degradation. This is consistent with the error patterns observed in our results, where residuals show greater magnitudes at lower elevations (see Figs. 10 and 11).

These consistent, elevation-dependent error patterns highlight the value of the controlled experimental approach we adopted. Three advances distinguish this study from Dutta et al. (2026): (1) their simulation-based prediction that a 1 m wall doubles position scatter is here empirically confirmed under controlled conditions with ground truth; (2) while they inferred diffraction from residuals alone, we directly compare residuals against theoretical knife-edge values, validating the physical mechanism; (3) our near-field (1 m) SNR data reveal that the KED model fails at grazing incidence–a limitation their qualitative SNR analysis did not capture. Collectively, these controlled-experiment results translate into quantifiable, validated error characteristics.

Conclusion and future work

High-precision, real-time GNSS applications–such as the guidance of excavators and cranes–depend on reliable second-by-second positioning. Operators typically mitigate errors using an elevation cutoff angle of 10° to 15°. Yet, in these cluttered environments, signal interference from multipath and diffraction is common and often more severe than post-processing

studies in controlled settings can show. While multipath is a recognized issue, the impact of diffraction is frequently disregarded. Its effects, though short-lived, can be critical. Beyond causing simple signal loss, diffraction can lead to erroneous coordinate estimates by several centimeter or even decimeter without warning. Also, such applications often consider PDOP as a quality indicator. However, we show in this paper that while PDOP is a necessary criteria, in a diffractive environment, it is definitely not sufficient.

Diffraction represents a fundamental and often unaddressed limitation in the achievable accuracy of both RTK and Network RTK systems. While the findings in this paper are based on PPP and double-difference residuals, they point toward potential implications for RTK and Network RTK scenarios. Because the observed errors are linked to the antenna's local environment, they do not appear to fully cancel through double-differencing, even with a co-located station. In operational Network RTK, where reference stations are often sited on roof parapets or near building edges, such site-specific errors could plausibly propagate to the rover. The effect is expected to be more pronounced in dense urban canyons than in our controlled setup. Experimental verification in real-time RTK is planned as future work.

Based on the results shown in this paper, we conclude that while standard PPP is highly effective and uses models of global error sources (orbits, clocks, troposphere) but when faced with an unmodeled error like diffraction, the PPP engine incorrectly adjusts its estimated parameters to fit the data, leading to significant and erroneous position estimates. The position estimates are indeed twice as worse, when the wall is closest at 1 m distance, as predicted by Dutta et al. (2026) using simulated data. This experimental confirmation goes beyond previous work by providing quantitative error magnitudes with associated uncertainties and suggests a practical clearance guideline.

We also conclude that, the impact of diffraction from an obstacle (in this case a wall) is severely magnified when the receiver is close to it. The effect diminishes as the distance increases. When at 1 m distance, the wall casts a large shadow, affecting many satellites and causing large errors. These errors correspond to an additional path delay (positive residuals), can be larger than a decimeter in magnitude and substantially degrade the ambiguity resolution efficiency for the post-processed solution. At 3 m distance, the shadow is smaller, affecting fewer satellites, and the resulting positioning errors are correspondingly smaller. Moreover, signals from low-elevation satellites are more severely impacted by diffraction because they travel a longer path through the disturbed Fresnel zone. The analysis of SNR data provides physical proof that the signal is degraded due to the obstacle interfering with the first Fresnel zone, even when it is below the direct LOS. This diffraction effect is well modeled by the KED model. However, the KED model is insufficient to quantify near field grazing incidence.

Optimal Azimuth-Elevation Masks (OAEMs) provide a user-friendly method for determining elevation cutoffs that minimize diffraction-affected measurements. However, their practical implementation faces limitations: site-specific OAEMs may not be available for arbitrary obstacle configurations, and aggressive satellite masking can degrade Dilution of Precision (DOP) by excluding geometrically favorable satellites. The conventional approach of applying a universal 10° elevation cutoff is similarly inadequate, as diffractive effects from large or proximate obstructions can persist well beyond this threshold, particularly for vertical metallic structures. For practical field applications, establishing antennas at sufficient clearance distances from obstacles remains the most reliable strategy. Based on the results of our experiments (for a 0.8 m high wall), a distance of 4 m is suggested to minimize diffraction impact. This translates to ensuring the obstructive environment does not subtend an angle greater than 11° on the antenna. Readers are cautioned that this value is not a universal constant. It is subject to change with signal frequency, antenna pattern, type of obstruction and the surrounding environment. For more demanding accuracy requirements, larger clearance distances should be considered. Nevertheless, the 11° value offers a practical starting point for field operations when site-specific data are unavailable. This substantially reduces diffraction errors while retaining sufficient satellite geometry. Where physical separation is constrained, supplementary approaches such as diffraction-aware weighting schemes or multi-frequency signal combination may offer intermediate solutions. Future mitigation strategies may benefit from machine learning approaches that adaptively weight satellite observations based on real-time obstruction geometry and signal quality metrics. As discussed in Sect. Modeling signal-to-noise ratio, SNR is a good indicator of the obstruction geometry around an antenna. Such systems could dynamically balance the competing objectives of minimizing diffraction effects while maintaining favorable satellite geometry, potentially overcoming the limitations of static elevation masks in complex operational environments.

Ultimately, these errors are inseparable from the antenna's local environment and are not automatically mitigated by standard processing software. Therefore, an important direction for future work is the development of robust, real-time capable models and mitigation strategies that explicitly account for diffraction. Addressing this challenge is essential for pushing the boundaries of achievable measurement uncertainty in demanding GNSS applications like RTK and PPP. We intend to study the limitation of KED model in modeling near-grazing and near-field diffraction conditions further. Also, role of Fresnel zones on GNSS signal diffraction will be studied in detail as a future work to this research.

Acknowledgements The authors acknowledge the support of Trafikverket for the funding provided through the Stomnät i Luften (SiL 2.0). The authors acknowledge the support of Lantmäteriet for providing the receivers and the antenna for the experiment. The authors also acknowledge the support of Technical Support Group (TSG) at the Onsala Space Observatory for providing invaluable support for setting up the experiments with the wall.

Author contributions UD: Conceptualization, Methodology, Investigation, Data Curation, Validation, Formal Analysis, Visualization, Writing—Original Draft, Writing—Review and Editing. JMJ: Resources, Supervision, Writing—Review and Editing. RH: Supervision, Writing—Review and Editing. SEGB: Writing—Reviewing. CR: Writing—Review and Editing. All authors have read and agreed to the published version of the manuscript.

Funding Open access funding provided by Chalmers University of Technology. This work is part of a PhD project funded by RISE Research Institutes of Sweden. Funding has also been provided by Trafikverket through the Stomnät i Luften (SiL 2.0) project grant number TRV 2018/111087, 2019.

Data availability The data that support the findings of this paper are available upon reasonable request.

Code availability The software code for generating the findings of this paper are available upon reasonable request.

Declarations

Conflict of interest No conflict of interest.

Ethical approval Not applicable.

Consent for publication Yes.

Open Access This article is licensed under a Creative Commons Attribution 4.0 International License, which permits use, sharing, adaptation, distribution and reproduction in any medium or format, as long as you give appropriate credit to the original author(s) and the source, provide a link to the Creative Commons licence, and indicate if changes were made. The images or other third party material in this article are included in the article's Creative Commons licence, unless indicated otherwise in a credit line to the material. If material is not included in the article's Creative Commons licence and your intended use is not permitted by statutory regulation or exceeds the permitted use, you will need to obtain permission directly from the copyright holder. To view a copy of this licence, visit http://creativecommons.org/licenses/by/4.0/.

References

Bertiger W, Bar-Sever Y, Dorsey A et al (2020) GipsyX/RTGx, a new tool set for space geodetic operations and research. Adv Space Res 66(3):469–489. https://doi.org/10.1016/j.asr.2020.04.015

Bradbury J (2007) Prediction of urban GNSS availability and signal degradation using virtual reality city models. In: Proceedings of the 20th international technical meeting of the satellite division of the institute of navigation (ION GNSS. Fort Worth, TX, pp 2696–2706

Breitsch B, Morton YT, Rino C et al (2020) GNSS carrier phase cycle slips due to diffractive ionosphere scintillation: simulation and characterization. IEEE Trans Aerosp Electron Syst 56(5):3632–3644. https://doi.org/10.1109/TAES.2020.2979025

Brunner FK, Hartinger H, Troyer L (1999) GPS signal diffraction modelling: the stochastic SIGMA-δ model. J Geodesy 73(5):259–267. https://doi.org/10.1007/s001900050242

CDDIS (2026) IGS data. https://cddis.nasa.gov/archive/gnss/data/daily/2026/100/

Dach R, Andritsch F, Arnold D, et al (2015) Bernese GNSS software version 5.2. https://doi.org/10.7892/boris.72297

Dutta U, Johansson J (2023) Multi-constellation/multi-frequency GNSS signal degradation due to foliage and reflective environments. In: Engineering proceedings 54(1). https://doi.org/10.3390/ENC2023-15454

Dutta U, Johansson J, Haas R (2026) Investigating the impact of diffraction on GNSS carrier phase measurements. J Geodesy 100(4):25. https://doi.org/10.1007/s00190-026-02045-w

Fan K, Ding X (2006) Estimation of GPS carrier phase multipath signals based on site environment. J Glob Position Syst 5:22–28. https://doi.org/10.5081/jgps.5.1.22

Groves PD, Jiang Z (2013) Height aiding, C/N0 weighting and consistency checking for GNSS NLOS and multipath mitigation in urban areas. J Navig 66(5):653–669. https://doi.org/10.1017/S0373463313000350

IGS (2018) RINEX: the receiver independent exchange format version 3.04. RINEX working group and RTCM-SC104, available at https://files.igs.org/pub/data/format/rinex304.pdf

McGraw GA, Groves PD, Ashman BW (2020) Robust positioning in the presence of multipath and NLOS GNSS signals. https://doi.org/10.1002/9781119458449.ch22

Nicolás ML, Smyrnaios M, Schön S, et al (2012) Investigation of diffraction effects in GNSS using ray tracing channel modelling: preliminary results. In: 2012 6th European conference on antennas and propagation (EUCAP), pp 3154–3158, https://doi.org/10.1109/EuCAP.2012.6206167

Orfanidis SJ (2002) Electromagnetic Waves and Antennas. Rutgers University, New Brunswick, NJ, http://leipper.org/manuals/zip-fill/www.ece.rutgers.edu/~orfanidi/ewa/ch17.pdf

Panicciari T, Soliman MA, Moura G (2017) Evaluation of a GNSS receiver performance in different multipath environments with a novel real-time multipath simulation system. In: Proceedings of the 30th international technical meeting of the satellite division of the institute of navigation (ION GNSS+ 2017), Portland, Oregon, pp 427–435, https://doi.org/10.33012/2017.15199

Petit G, Luzum B, (eds.) (2010) IERS conventions. IERS technical note 36, international earth rotation and reference systems service (IERS), Frankfurt am Main, Germany, https://www.iers.org/IERS/EN/Publications/TechnicalNotes/tn36.html, 179 pp

Rappaport TS (1996) Wireless communications: principles and practice, 1st edn. Prentice Hall, Upper Saddle River, NJ

Ren H, Li G, Geng J, et al (2023) Multipath hemispherical map model with geographic cut-off elevation constraints for real-time GNSS monitoring in complex environments. GPS Solut 27(4). https://doi.org/10.1007/s10291-023-01530-5

Schaper A, Ruwisch F, Schön S (2022) Diffraction modeling for improved 3DMA GNSS urban navigation. In: 35th International technical meeting of the satellite division of the institute of navigation, ION GNSS + 2022, pp 1902–1916, https://doi.org/10.33012/2022.18541

Suzuki T, Kubo N (2012) GNSS positioning with multipath simulation using 3D surface model in urban canyon. Proceedings of the 25th International Technical Meeting of the Satellite Division of The Institute of Navigation (ION GNSS 2012. Nashville, TN, pp 438–447

Xi R, Xu D, Jiang W et al (2023) Elimination of GNSS carrier phase diffraction error using an obstruction adaptive elevation masks

determination method in a harsh observing environment. GPS Solut 27(3):139. https://doi.org/10.1007/s10291-023-01473-x

Xi R, Han L, Chen Q et al (2025) Numerical modeling and analysis of GNSS carrier-phase diffraction error in occlusion environments. J Geodesy 99(4):32. https://doi.org/10.1007/s00190-025-01956-4

Zhang G, Hsu LT (2021) Performance assessment of GNSS diffraction models in urban areas. Navigation 68(2):369–389. https://doi.org/10.1002/navi.417

Zhang Z, Li Y, He X et al (2022) A composite stochastic model considering the terrain topography for real-time GNSS monitoring in canyon environments. J Geodesy 96:79. https://doi.org/10.1007/s00190-022-01660-7

Zimmermann F, Eling C, Kuhlmann H (2017) Empirical assessment of obstruction adaptive elevation masks to mitigate site-dependent effects. GPS Solut 21(4):1695–1706. https://doi.org/10.1007/s10291-017-0650-5

Zou X, Fu R, Tang J et al (2023) Multipath error mitigation method considering NLOS signal for high-precision GNSS data processing. GPS Solut 27(4):175. https://doi.org/10.1007/s10291-023-01498-2

Publisher's Note Springer Nature remains neutral with regard to jurisdictional claims in published maps and institutional affiliations.



Uttama Dutta is a researcher at RISE Research Institutes of Sweden in the department of Mesurement SCience and Technology. She received a Licentiate degree in 2024 from Chalmers University of Technology, Sweden and is presently pursuing a PhD in the unit of Space Geodesy and Geodynamics at the same university. Her research focuses on enhancing the reliability of GNSS carrier phase measurements for precise positioning applications. In particular, she investigates GNSS error sources such as ionosphere and antenna environment.



Jan M. Johansson RISE Research Institutes of Sweden and adjunct Professor of Space Geodesy at Chalmers University of Technology. He is the director of the Swedish National Metrology Institute (NMI) hosted at RISE and the Swedish representative in the international metrology community. His research interest focus on space geodetic techniques and applications of Global Navigation Satellite Systems (GNSSs).`



Rüdiger Haas is a Full Professor of Space Geodesy at Chalmers University of Technology. He is the Head of the Research Group for Space Geodesy, and responsible for the geoscience activities at the Onsala Space Observatory, His research interests focus on space geodetic techniques, such as Global Navigation Satellite Systems (GNSSs), including GNSS reflectometry, and very long baseline interferometry (VLBI).



Sten Bergstrand RISE Research Institutes of Sweden, PhD in Space Geodesy. Metrologist and Senior Researcher in the Dimension and Position unit at the Department of Measurement Technology at RISE with focus on GNSS applications. Swedish representative to the European Association of National Metrology Institutes Technical Committee for Length. Chair of CCL Working Group on the CIPM MRA.



Carsten Rieck Lic Eng. Electrical Engineering, Chalmers University of Technology, time metrologist, since 2000 at SP/RISE Time and Optics. Responsible for TWSTFT development and operation at RISE. Research focus is on space geodetic methods for time and frequency metrology, with focus on GNSS. Works also with the RISE network time services (NTP, NTS, PTP, WR) and their metrological traceability. Since 2005, he has been member of the CCTF WG on TWSTFT and is since 2021 co-chair of this group.